Oceanic Transports of Heat and Salt from a Global Model and Data

by

Elise Olson

B.S., Earth, Atmospheric, and Planetary Sciences
Massachusetts Institute of Technology, 2006

Submitted to the Department of Earth, Atmospheric, and Planetary Sciences
in Partial Fulfillment of the Requirements for the Degree of
Master of Science in Climate Physics and Chemistry

at the
Massachusetts Institute of Technology
September 2006

Signature of Author.....
Department of Earth, Atmospheric, and Planetary Sciences
August 28, 2006

Certified by.....
Carl I. Wunsch
Cecil and Ida Green Professor of Physical Oceanography
Thesis Supervisor

Accepted by.....
Maria T. Zuber
E. A. Griswold Professor of Geophysics
Chair, Department of Earth, Atmospheric, and Planetary Sciences

Oceanic Transports of Heat and Salt from a Global Model and Data

by

Elise Olson

B.S., Earth, Atmospheric, and Planetary Sciences
Massachusetts Institute of Technology, 2006

Submitted to the Department of Earth, Atmospheric, and Planetary Sciences
in Partial Fulfillment of the Requirements for the Degree of
Master of Science in Climate Physics and Chemistry

ABSTRACT

A state estimate produced by ECCO-GODAE from a global one-degree model and data spanning the years 1992-2005 is analyzed in terms of transports of volume, temperature, and freshwater. The estimate is assessed to be sufficiently close to observations to merit analysis. The methods of analysis are similar to those of Stammer et al. (2003). The longer time period allows trends to be measured with greater confidence. Time mean flow characteristics demonstrate agreement with previous estimates. The strength of the ACC (146±5Sv) is larger than in the Stammer et al. (2003) state estimate, but is within the range of other estimates. A twelve-year decreasing trend is observed in the strength of the ACC of approximately 0.88Sv/year. The Indonesian throughflow transport of 11±2Sv is within the expected range. There is also a decreasing twelve year trend in the strength of the ITF of 0.065Sv/year. The ITF is stronger in boreal summer than boreal winter by approximately 4Sv. A strong annual cycle is present in the transport record on most sections, but higher frequency variability is also present. Most temperature transport variability results from velocity fluctuations, except in the Southern Ocean where temperature fluctuations are more important. Recommended further work includes a more detailed analysis of variability in this state estimate.

Thesis Supervisor: Carl Wunsch
Title: Cecil and Ida Green Professor of Physical Oceanography

Table of Contents

List of Tables

List of Figures

1. Introduction

Ocean currents and thermodynamics are of great relevance to the study of meteorology and climate because of the intricate interactions between ocean and atmosphere. For example, according to theory, the tropical ocean can act as a heat reservoir fueling hurricanes, and changes in the overturning circulation of the North Atlantic may be associated with ice ages. If not for the North Atlantic circulation, European history might have taken a different course because the continent would be colder and less habitable.

Great size and complexity, long timescales, and sparse observational data are only a few of the challenges faced by oceanographers. One approach to the problem is the development and study of general circulation models, or GCMs. These highly complex numerical models are designed to take into account as much dynamical theory and observational data as contemporary computing power allows. Due to computational limitations, only a limited number of grid points can be used in a model. However, some important ocean processes occur on scales smaller than the allowed model resolution. These processes must be represented by parameterizations, which can introduce errors into the model. In addition, the ocean system may be inherently chaotic, so that tiny errors present in all measurements used to calculate the initial state of the system could lead to highly inaccurate predictions.

Another approach to the study of ocean circulations and other properties is direct observation. The obvious limitation of this method is that, due to limited resources, only small areas of the oceans may be observed for limited periods of time. Much of the deep ocean is inaccessible to measurements. Since fluctuations in the oceans are present on all time scales, studies based on a few months of data are likely to be significantly biased.

State estimation combines the advantages of both of the previous methods at the expense of increased computational load. A full ocean general circulation model is constrained by observational data. In this way, a maximum amount of available information can be synthesized into a single description of the ocean's circulation, the state estimate.

The state estimate to be analyzed in the following chapters is one stage of an ongoing process. However, it also results from many years of work including several initiatives and collaborations. The development of the state estimate began with the creation of the Estimating the Circulation and Climate of the Ocean (ECCO) Consortium by scientists at the Jet Propulsion Laboratory (JPL), Massachusetts Institute of Technology (MIT), and Scripps Institution of Oceanography (SIO) in 1999, under the National Ocean Partnership Program (NOPP) with funding from the National Science Foundation (NSF), the National Aeronautics and Space Administration (NASA), and the Office of Naval Research (ONR) (Papadopoulos, 2005). The work continues in support of the Global Ocean Data Assimilation Experiment as ECCO-GODAE (Heimbach and Evangelinos, 2006), with support from the NOPP, NSF, NASA and the National Oceanic and Atmospheric Administration (NOAA) (Papadopoulos, 2005). ECCO-GODAE progresses toward the creation of a near-real time, three-dimensional, global estimate of the state of the ocean by integrating the products of many other efforts. The contributions to the ECCO-GODAE state estimate include the MITgcm developed under the Climate Modeling Initiative (*About CMI: MIT's Climate Modeling Initiative*), the extensive data, including physical and chemical observations from moored and drifting instrumentation as well as global satellite observations, collected during the World Ocean Experiment (WOCE) that lasted from 1990 to 2002 (*The World Ocean Circulation Experiment (WOCE) 1990-2002*), TOPEX/POSEIDON and JASON altimeter observations, and the temperature, salinity, and velocity data continuously output by Argo, a global array of 3000 floats in the upper 2000m of the ocean (Argo, 2006).

To obtain the state estimate, a version of the MITgcm is constrained by altering initial conditions and surface forcing fields to minimize the least-squares model-data misfits (Stammer et al., 2002a). The advantage of this method over less rigorous techniques such as "nudging" is the avoidance of inconsistencies such as internal sources and sinks of conserved quantities including momentum, heat, and fresh water (Stammer et al., 2002a). The state estimate continues to evolve as new data and other improvements become available, but the version discussed here is stable enough and

close enough to observational data to merit analysis of its characteristics and implications (Wunsch and Heimbach, 2006).

The analysis to be presented focuses on the volume, temperature, and fresh water transports and any apparent trends in those quantities at several locations spread across the globe based on one recent version of the ECCO-GODAE (Global Ocean Data Assimilation Experiment) state estimate. A more accurate description of these transports and the associated air-sea surface fluxes may further understanding of the ocean's role in climate. In particular, it could be used to estimate the timescales on which chemicals can penetrate the deep oceans, trends in ocean temperature and the ocean's role as a heat reservoir, or indications of climate change. In addition, the analysis may be useful in further improving the state estimate in future iterations, possibly pointing to areas most in need of further observational data or more developed theory.

Increasing computer power, more complete observational data coverage and error estimates, and evolution of models and assimilation methods are all expected to result in improved state estimates in the future (Stammer et al., 2002b). Eventually, a state estimate might be developed that is precise and accurate enough to be useful as a climate-forecasting tool (Stammer et al., 2002a). Such a state estimate might be applied to the study of the ocean's capacity to store carbon or used in models of biological activity (Stammer et al., 2002a). It could provide knowledge of currents that would aid in search and rescue, prediction of iceberg paths or trajectories of oil spills or other contaminants, and optimization of shipping routes (Stammer et al., 2002a). It might even be of use in the study and prediction of hurricane formation and trajectories.

2. Literature Review

The ocean's role in climate regulation includes the transport of energy, freshwater, oxygen and nutrients and their transfer between ocean and atmosphere (Ganachaud and Wunsch, 2002). Although the ocean's meridional energy transport may account for as little as 10% of the total heat transport, that amount is still significant to the climate system (Wunsch, 2005). Thus, the calculation of transports is of great scientific interest. Information about property transports and more could be obtained from an accurate estimate of the state of the world's oceans. Such an estimate is becoming more and more realistic as research programs such as WOCE and the Tropical Ocean Global Atmosphere Program (TOGA) contribute to the development of a global observing system (Stammer et al., 2002a).

Stammer et al. (2002) mention some of the goals and challenges of state estimation, the process of assimilating data and models. The immediate goal is to obtain the best possible estimate of the ocean circulation based on current knowledge. Compared to similar atmospheric studies, oceanic state estimation is less directed toward prediction and more aimed at estimating current and recent conditions to gain understanding of ocean processes and dynamics. Also, smaller dynamical scales are important, so higher resolution is necessary, requiring more computing power.

A description of the model used in this state estimate can be found in *MIT Climate Modeling Initiative* (2004) but is summarized here. The MITgcm, developed by MIT's Climate Modeling Initiative (CMI) under the direction of John Marshall (*About CMI: MIT's Climate Modeling Initiative*), was designed to be versatile; the same algorithm may be used to model atmosphere or ocean by using the appropriate equation of state, forcing, and parameterizations. The model can be further adapted for use on small, nonhydrostatic scales or large, hydrostatic scales. It is based on the incompressible Navier-Stokes equations, but can include non-hydrostatic terms important in mixing. Finite volume methods and orthogonal curvilinear coordinates in the horizontal allow for use of innovative spherical grids. The finite volume shaved cell grid allows for the specification of arbitrary coastline and bottom topography (Marshall et al., 1997). Three types of upper boundary conditions are available in the MITgcm: a rigid-lid

approximation, a linear free-surface allowing propagation of surface gravity waves, and a non-linear free surface, in which the geometry of upper level finite volumes varies in time (*MIT Climate Modeling Initiative, 2004*). An adjoint, useful in state estimation and sensitivity studies, can be produced using automatic differentiation.

The Boussinesq approximation used in the model is valid because density variations are small compared to the background reference density. The nonhydrostatic, incompressible Boussinesq equations used in the height coordinate mode of the model can be expressed:

$$\rho_0 D_t \vec{v} + 2\Omega \times \rho_0 \vec{v} + g\rho\hat{k} + \nabla p = \vec{F}, \quad (1)$$

$$\rho_0 \nabla \cdot \vec{v} = 0, \quad (2)$$

$$\partial_t \eta + \nabla \cdot (H + \eta)\vec{v}_h = P - E, \quad (3)$$

$$D_t \theta = Q_\theta, \quad (4)$$

$$D_t s = Q_s, \quad (5)$$

$$\rho = \rho(s,\theta,p), \quad (6)$$

where $\vec{v}$ is the three dimensional velocity vector, p is pressure, ρ is in-situ density, ρ_0 is a constant reference density, η is the displacement of the free-surface from resting sea-level, θ is potential temperature, s is salinity, g is the gravitational acceleration, H is the bottom depth, and $\vec{F}$, $P-E$, Q_θ, and Q_s are arbitrary forcing fields.

Marshal et al. (1997) describe an implementation of the MITgcm for the ocean. It is an efficient, nonhydrostatic model that makes use of parallel computers, with alternating phases of "local computation and global communication". The dynamics approach the Navier Stokes equations as resolution increases. The pressure field is divided into surface, hydrostatic, and nonhydrostatic components. As the horizontal motions become much larger than the vertical motions, the motion becomes increasingly hydrostatic and the 3-d Poisson operator is dominated by the vertical axis.

The model does not allow normal flow through solid boundaries. At land boundaries, the diffusive flux of heat and salt is set to zero. Wind stress and heat and salt fluxes are prescribed at the surface. The model's grid is made up of parallelograms with

velocity components normal to the faces. In contrast, pressure, density, temperature, and salinity are zone quantities specified as volume averages over a cell and are therefore specified at the center of the cell rather than the faces. The Coriolis term must be spatially averaged because the velocity components are staggered in space. The model has potential for use on local or global scales and could be coupled to a similarly developed atmospheric model.

Stammer et al. (2002b) described a three-dimensional oceanic state estimate derived from a combination of observational data and a model based on the Marshall et al. (1997) implementation of the MITgcm. The paper described the methods used to obtain the state estimate and assesses the level of agreement between the solution and its constraints as well as independent observational data. Key points are summarized here.

Data employed in the Stammer et al. (2002b) assimilation included "monthly mean [Levitus et al., 1994a, 1994b] hydrographic climatology, monthly mean [Reynolds and Smith, 1994] sea surface temperature (SST) fields, the altimetric measurements from TOPEX/Poseidon (T/P), ERS-1, and ERS-2, and daily surface forcing over the time interval 1992-1997," as well as the EGM96 geoid model (Lemoine et al., 1997, cited by Stammer et al., 2002b).

Because the model employed the Boussinesq approximation, it conserved volume rather than mass (Stammer et al., 2003). It had a 2° resolution in latitude and longitude, extended from 80°S to 80°N, and included 22 vertical levels (Stammer et al., 2002b). Boundary conditions were free-slip at the bottom and non-slip on lateral walls. The model did not include river run-off or an accurate representation of the salt flux out of the Mediterranean, but the effects were approximated through adjustments to the surface forcing fields (Stammer et al., 2003). The model was run from 1992 to 1997 and was stepped forward in time using the hydrostatic internal pressure and the vertical velocity calculated from continuity (Stammer et al., 2002b). Uncertainties were assumed to be due to initial conditions and surface forcing fields rather than model error (Stammer et al., 2003).

An algebraic expression of a general circulation model is

$$\mathbf{x}(t+1) = \mathcal{L}\left[\mathbf{x}(t), \mathbf{B}\mathbf{q}(t), \boldsymbol{\Gamma}\mathbf{u}(t)\right], \tag{7}$$

where $\Delta t = 1$ is the time step, $\mathbf{x}(t)$ is the state vector, with $\mathbf{x}(t_0)$ the vector of initial conditions, $\mathbf{B}$ is a matrix that maps $\mathbf{q}(t)$ to the grid, $\mathbf{q}(t)$ represents externally specified boundary conditions, sources, and sinks, $\boldsymbol{\Gamma}$ is a matrix that maps $\mathbf{u}(t)$ to the grid, $\mathbf{u}(t)$ represents unknown "controls", and $\mathcal{L}$ is a nonlinear operator that steps the model forward in time (Stammer et al., 2002b). The matrix $\mathbf{u}(t)$ can be divided into components,

$$\mathbf{u}(t)^T = \left[\mathbf{u}_0^T, \mathbf{u}_f^T, \boldsymbol{\varepsilon}^T\right], \tag{8}$$

where the components represent errors in initial conditions, external forcing fields, and internal model physics, respectively.

The relationship between a measured quantity and the state vector can be expressed as

$$\mathbf{y}(t) = \mathbf{E}(t)\mathbf{x}(t) + \mathbf{n}(t), \tag{9}$$

where $\mathbf{y}(t)$ is the observed quantity, $\mathbf{E}(t)$ is the "observation matrix" relating the model state vector to the observed quantity, and $\mathbf{n}(t)$ represents noise.

The model is constrained by minimizing the model-data misfit within uncertainties by adjustments to initial conditions, model parameters, and forcing fields. Once the optimal values are found, the GCM is time-stepped forward. The assimilation problem is formulated as a least squares problem in which a quadratic cost function is minimized, subject to model constraints, by modification of the control variables. The cost function may be written

$$J = \sum_{t=1}^{t_f} \left(\mathbf{y}(t) - \mathbf{E}(t)\tilde{\mathbf{x}}(t)\right)^T \mathbf{W}(t)\left(\mathbf{y}(t) - \mathbf{E}(t)\tilde{\mathbf{x}}(t)\right), \tag{10}$$

where $\tilde{\mathbf{x}}(t)$ is the estimate of the state vector. $W(t)$ is a weight function, usually the inverse variances of the estimated data error.

In order to enforce the model it is appended to the cost function:

$$L = J + \mathbf{u}_0^T \mathbf{Q}_0^{-1} \mathbf{u}_0 + \sum_{t=0}^{t_{f-1}} \left[\boldsymbol{\varepsilon}^T(t) \mathbf{Q}_\varepsilon^{-1}(t) \boldsymbol{\varepsilon}(t) + \mathbf{u}_f^T(t) \mathbf{Q}_f(t)^{-1} \mathbf{u}_f(t) \right]$$

$$-2 \sum_{t=0}^{t_{f-1}} \boldsymbol{\mu}(t+1)^T \left\{ \mathbf{x}(t+1) - \mathcal{L}\left[\mathbf{x}(t), \mathbf{B}\mathbf{q}(t), \boldsymbol{\Gamma}\mathbf{u}(t) \right] \right\} \qquad (11)$$

$\mathbf{Q}(t)$ represents uncertainty in the model dynamics (Stammer et al., 2002b). $\mathbf{Q}(t)$ may be separated into components,

$$\mathbf{Q}^T = \left[\mathbf{Q}_0^T, \mathbf{Q}_f^T, \mathbf{Q}_\varepsilon^T \right], \qquad (12)$$

representing the contributions of initial conditions, external forcing, and internal model physics, respectively. $\boldsymbol{\mu}(t)$ represents Lagrange multipliers and t_f is the final time step. A stationary value of L, which is a constrained minimum of the cost function J, is computed by setting the derivatives of L with respect to $\mathbf{u}, \mathbf{x}$, and $\boldsymbol{\mu}$ equal to zero.

The advantage of this method over others such as nudging or objective mapping is that it can be implemented in a rigorous manner so that the estimate is consistent with the physical model and there are no artificial sources or sinks.

The adjustments made to the initial temperature and salinity fields and to the forcing fields were determined to be consistent with hydrographic climatology and meteorological analyses within accepted uncertainties, although some changes were believed to be the result of compensation for low model resolution. Changes made to the initial temperature fields extended far below 435m, indicating a connection between surface elevation and deep ocean processes.

The constrained model was closer to sea surface height and hydrographic observations than was the control run. In the Stammer et al. (2002b) solution, heat uptake occurred at most eastern boundary currents. Net evaporation was found over the eastern side of all subtropical gyres, while net precipitation occurred in the tropics and at most high-latitude locations. All major current systems were found in the solution but were smoother than they ought to be, due to the coarse model resolution. Some eddy-like features were present. There was a deep western boundary current along the entire North Atlantic, a weaker but similar boundary current in the Northern Pacific, a strong southward western boundary current in the Southern Pacific, and another in the Indian

Ocean in the Southern Hemisphere. Estimated temperature and salinity profiles were consistent with known water mass distributions within uncertainties. Ekman convergence and equatorial upwelling were found in the tropics, and large areas of Ekman pumping and suction were found over much of the ocean.

The state estimate was expected to more accurately represent variability than a time average state due to uncertainties in model physics and surface forcing as well as the short length (1992-1997) of the state estimate in time. Annual cycles were characterized by seasonal heating and circulation changes. Annual cycles in sea surface height were determined to be associated more closely with cycles in water mass distribution than with heat content. Anomalies in temperature and flow on annual time-scales generally coincided.

Stammer et al. (2002b) noted that the computation of error bars was highly desirable but not feasible at the time of the study. The solution was compared to constraining and withheld data instead. Outlying residuals were as large as ±50cm in mean surface height, which often coincided with islands and topographic features. These extreme values were quite large compared to earlier error estimates, but the root-mean-square error was considered acceptable. Stammer et al. (2002b) suggest the outlying sea surface height residuals may have resulted from errors in the geoid rather than model error. The errors in salinity compared to WOCE climatology were slightly greater in the constrained model than the unconstrained model, but were still within error bounds. The uncertainties at levels above 1000m may have been underestimated initially.

Stammer et al. (2002b) stated that the most important result of the study was that a self-consistent state estimate could be produced from a model and data. The estimate was successful in reproducing large-scale circulation patterns in many areas, including some features that are absent in most models of similar resolution. Compared to the unconstrained model, the state estimate was closer to both the constraints and withheld data. Stammer et al. (2002b) also pointed out that the solution found was not necessarily the "global minimum" but that another separate solution was unlikely given the geographical coverage of the climatologies and continuous observing. They suggested that the next step would be to estimate global heat and freshwater fluxes and variations in flow fields on timescales of a day. Also, upwelling and potential vorticity fluxes could

be assessed. Improved eddy parameterization and model resolution were important goals for future state estimates.

Stammer et al. (2003) built on the 2002 study; information from the 2003 paper follows. The 2003 state estimate differed from the 2002 estimate in that the time period was extended to 1992-2000 and additional constraints were employed to prevent model drift. The first and last year temperature and salinity were not allowed to differ by more than 10% of their uncertainty. Transients were observed in the first year; in particular, there were large vertical velocities near steep topography. Therefore, the results were analyzed beginning at 1993.

The model did not allow volume exchange across the Arctic. Therefore, the Atlantic was a closed basin and could have no net volume fluxes. In contrast, net volume fluxes were found in sections across the Southern ocean and in sections connecting Australia to other continents. Stammer et al. (2003) found a mean Indonesian Throughflow (ITF) of 11Sv, in good agreement with independent estimates. East of Madagascar, an average of 5Sv flowed north across 20°N in the Indian Ocean; these 5Sv as well as the 11Sv of the ITF returned south through the Mozambique Channel, which had a total mean southward transport of 16Sv. The mean transport of the Antarctic Circumpolar Current (ACC) was 124Sv, which was in agreement within error bounds of several independent estimates. The eastward transport between Australia and Antarctica was a combination of the ACC and the return of the ITF. The recirculation of the ITF around Australia was supported by the previous results of Macdonald and Wunsch (1996) and Ganachaud and Wunsch (2000) as cited in Stammer et al. (2003).

High-frequency variability of volume transports in closed basins indicated storage effects. Variations in heat storage contributed to sea level changes. Variations with frequencies shorter than 30 days were "dominated by the rapid wind-induced Ekman transport and an associated barotropic return flow" (Stammer et al., 2003). Variations were also found in sections with net transport; a seasonal cycle was present in the Indian Ocean east of Madagascar at 20°N with a maximum flow of 10Sv between October and December and almost no flow during boreal winter. A circulation was present around Madagascar with both mean and time-varying components. The variability in the time series demonstrated that long-term mean circulations could not be calculated from

measurements lasting only one year. The model should actually have underestimated the high-frequency fluctuations because of its low resolution.

Distinguishing between real physical changes and model drift was a challenge. The South-Pacific/Indian Ocean system was "spinning up" by about 1.5 Sv while the ACC weakened by 2.5 Sv.

The mean temperature transport of the ITF was 1.1 W, directed from the Pacific to the Indian. An average of 0.14 PW was transported from the Indo-Pacific system to the Atlantic through the Drake Passage. The heat transport time series showed seasonal and interannual variability. When heat transports were analyzed according to depth, the shallow region had the largest variability, associated with near-surface Ekman transports.

Temperature transport patterns were similar in the North Pacific and North Atlantic, but there was not a deep southward western boundary current in the Pacific. There were large southward transports on both sides of Madagascar. There was large variability near steep topography. Most of the variations in heat transport below 500m were due to changes in volume transport. However, temperature variations became more important toward high latitudes.

In the eastern North Pacific, horizontal transports converged zonally and diverged meridionally, while net surface heat transport was positive. ENSO effects were present in the South Pacific, particularly in 1997 when there was zonal convergence and meridional divergence on the western side. Changes in net ocean heat content were smaller than the net surface heat transport fields suggested. Heat content increased outside the tropics, particularly over the Southern Ocean. Over the Kuroshio, salinity changes were large; temperature changed more obviously over the central Pacific, as was expected from a Pacific Decadal Oscillation. Vertical numerical diffusion did not erode temperature and salinity structures significantly. Near source regions of deep water masses, there were large changes in temperature and salinity. Warming in the deep ocean varied significantly spatially and may have had short advective timescales near water mass source regions.

Horizontal transports are integrals of the products of absolute velocities, property concentrations and density (Ganachaud and Wunsch, 2002). Vertical transports are

products of vertical velocities, density and concentration added to diffusion (Ganachaud and Wunsch, 2002). Freshwater flux can be estimated by the equation

$$F_W = \int_0^L \int_{-H}^0 \rho v \left(1 - \frac{S}{S_0}\right) dz dx, \qquad (13)$$

where S is salinity and S_0 is a reference salinity (Stammer et al., 2003). The global mean freshwater transports were southward north of 20°S, except near 10°N where they were close to zero. South of 20°S, freshwater transports were on average directed northward. A divergence resulted at 20°S that would have had to have been balanced by atmospheric moisture transport.

Net surface heat and freshwater fluxes based on both estimated surface flux fields and divergences of meridional transports were plotted and compared. The convention used was that positive divergence corresponded to oceanic heat gain, and convergence corresponded to oceanic heat loss (Ganachaud and Wunsch, 2003). The estimates were similar but not exactly equal, which indicated that the model was not in equilibrium (Stammer et al., 2003). The authors noted a warming pattern in regions of the Southern Ocean, especially near the Atlantic and Indian Oceans. In the southern hemisphere, heat was gained over the Atlantic and lost over the Indian and Pacific.

Stammer et al. (2003) concluded that the quality of flow estimates was limited by the low model resolution, so the most important results were that such computations were feasible and could be used for quantitative estimates of things that could not be directly observed. Time-average transports of heat and freshwater agreed with independent estimates from box inversions in most regions, especially the southern hemisphere. The ocean state represented a balance between surface fluxes of momentum, heat, and freshwater. A circulation around Australia was confirmed. The ACC estimate of 124Sv was in good agreement with observations and previous estimates. Future computations would be investigated including a 1° grid, mixed layer dynamics, and the Gent-McWilliams mixing scheme, among other things.

Wunsch and Heimbach (2006), to be sumarized next, discuss trends in the North Atlantic meridional overturning circulation and heat fluxes across 26°N in the Atlantic based on ECCO-GODAE solution 2.177, "chosen because the misfit reduction had

largely ceased." ECCO-GODAE solution 2.177 will be the subject of analysis in this thesis as well. As in Stammer et al., 2002 and 2003, the "ECCO form" of the MITgcm (Marshall et al., 1997) is used (Wunsch and Heimbach, 2006). The important changes in the model from the 2002 and 2003 versions are the extension in time to 2004 and a finer, 1° spatial resolution.

Because the accuracy and precision of the model and data are not perfectly known, complete consistency between the data and solution will probably never occur. Each successive solution is the current best estimate based on the data and model used and the available error information. The estimate of the abyssal circulation is mainly determined by the requirement of consistency with the model. The major inconsistencies remaining between model and data concern ARGO temperature profiles in the far northeastern North Atlantic, southeastern South Pacific and Southern Ocean from 2003-2004.

Variability of ocean currents have been observed on all time scales, showing no spectral gaps. Trends must be distinguished statistically, therefore, from natural variability. In such a noisy system, the probability of finding exactly zero change is extremely small. In addition, low frequency variations may appear to be trends.

The dominant fluctuations in the volume transport at 26°N, of magnitude ±3Sv, are from the annual cycle and are associated with temporary water storage. These fluctuations would drown out any indication of an estimated 3mm/yr rise in sea level. Compared to other direct estimates, the heat flux of $(0.84\pm0.18)\times10^{15}$W is slightly small, but the error ranges do overlap. If there is a bias it may be due to the inability of a 1° resolution model to capture the temperature and velocity extremes present in the ocean; experiments have shown that if the resolution is reduced, the poleward heat flux found from the model decreases.

Wunsch and Heimbach (2006) found that the time-mean velocity structure at 26°N consists of an upper ocean northward flow above 1165m, an intermediate southward flow between 4450 and 1165m, and a varying abyssal flow below 4450m. The upper ocean flow of 13.2±1.8Sv is representative of the strength of the meridional overturning circulation (MOC). Wunsch and Heimbach (2006) observed an Antilles

current, western boundary current, and somewhat broad Gulf Stream in the flow field. There is a warming trend near 1000m in the eastern Atlantic, but cooling near the surface.

Distinguishing real trends from artificial model drift presents a problem. Models drift for a variety of reasons, including real physical changes, internal variability, numerical issues, and aliasing of high-frequency signals. Constraints on the ECCO-GODAE state estimate include requirements that initial and terminal values of some variables not differ by more than specified amounts; for example, the surface temperature may not vary by more than .83°C per decade. However, there is no indication that these constraints are restricting the trends seen in the solution. A trend in the volume flux above 1165m of -0.19±0.05Sv/yr was found, with the uncertainty calculated based on the assumption of a white noise spectral character. The calculated trend in net heat transport of $(-1.1\pm4.3)\times10^{12}$W/yr is indistinguishable from zero.

Wunsch and Heimbach (2006) concluded that any changes in the volume or heat transports at 26°N in the Atlantic were small and complex. The statistically significant decreasing upper-ocean trend in volume transport is counteracted by an intensification of flow at greater depths and was not associated with a statistically significant trend in meridional heat flux. These results lead to problems such as the physical cause of the volume transport trend, whether there is a true trend or low frequency fluctuation, why the heat flux is unaffected, and whether the trend is confirmed independently. Future estimates should make use of all available data and uncertainty estimates. Any attempts to extrapolate the results to long-term climate change should be extremely cautious.

3. Methods

The output of an assimilation of ECCO-GODAE solution 2.177 is analyzed in terms of velocity, temperature, and salinity fields and transports of volume, temperature, and freshwater across several transoceanic sections. All of these quantities are calculated and plotted using Matlab code written by Professor Carl Wunsch, Diana Spiegel, and the present author.

The assimilation output used is in the form of global horizontal velocity, temperature, and salinity fields, averaged monthly and spanning the time period 1992 to 2005. The first year is removed from the data to reduce the presence of transients in the analysis.

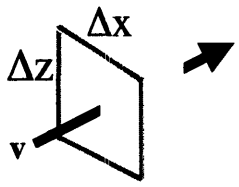

Figure 1. Diagram of grid geometry on sections. Δx is equal to one degree of latitude in a meridional section or one degree of longitude in a zonal section. Δz varies with depth.

Volume transports are calculated by multiplying the velocity normal to each grid-box by the area of the box and then summing over all the boxes that make up the section. Volume transports are calculated as

$$F_v = \sum_{i,k} v_{ik} \Delta x_i \Delta z_k \qquad (14)$$

where v is the velocity normal to the section, Δx is the length of the grid box along the section, and Δz is the height of the grid box (see Figure 1).

Temperature transports are calculated by multiplying each box's volume transport by its potential temperature and then summing over the boxes in the section. Because the conductivity of seawater is so small, the molecular heat flux across a section is generally negligible compared to the advective terms (Warren, 1999), so only the advective temperature transport is considered. The temperature transport is multiplied by the mean density and specific heat to convert to units of Watts.

$$F_q = \rho c_p \sum_{i,k} T_{ik} v_{ik} \Delta x_i \Delta z_k \qquad (15)$$

where ρ is density, c_p is specific heat, and T is potential temperature.

Warren (1999) derived an equation for the transport of energy across a section:

$$\int \rho E v d\sigma = \int \left(U + \tfrac{1}{2}c^2 + \varphi + \alpha p\right) \rho v d\sigma \approx \int \rho c_p T v d\sigma, \qquad (16)$$

where U is internal energy per unit mass, c is magnitude of velocity, φ is gravitational potential, α is specific volume, p is pressure, and $d\sigma$ is area element. As Warren (1999) pointed out, F_q is an even better approximation to the total energy than to the internal energy when the gravitation potential is referenced to the mean sea surface height. This is because in the equation for the total energy, the combined pressure and gravity-potential terms nearly cancel the pressure term that is neglected in the approximation to the internal energy (Warren, 1999).

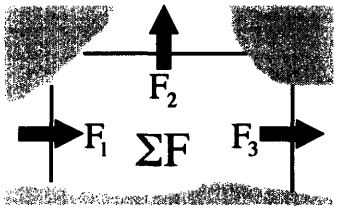

Figure 2. Diagram of sections that fully enclose a region. Gray areas represent land. Arrows represent direction of transports.

If there is net flow across a section, the temperature transport depends on an arbitrarily chosen constant reference temperature (Warren, 1999). However, if the net flow is zero, the reference temperature term drops out, and the temperature transport may be interpreted as a heat transport (Stammer et al., 2003). Alternatively, the section may be combined with others in such a way that the net flow across the combined sections is zero (Warren, 1999); for example, sections that together fully enclose a region with no net volume flux are combined in order to calculate the heat flux into or out of the region. Figure 2 shows such a region. The net flux into the region from the atmosphere is

$$\Sigma F = F_2 + F_3 - F_1. \qquad (17)$$

Sections may have net flow because they are open-ended or due to runoff or surface fluxes (Warren, 1999); however, net flow resulting from runoff or surface fluxes is usually small enough to be ignored.

As in Stammer et al. (2003), the temperature transport is divided into components based on mean velocity and temperature and variations in order to determine whether temperature or velocity variations contribute most of the variability at a particular section. Relation (15) may be expressed as an integral:

$$F_q = \int_0^L \int_{-D}^0 \rho c_p v T dz dx \qquad (18)$$

(Stammer et al., 2003), where L is the length of the section and D is the depth of the section. Substitute into equation (18)

$$T = \overline{T} + T', \qquad (19)$$

where $\overline{T}$ is the time mean temperature and T' is the departure from the time mean temperature, and

$$v = \overline{v} + v', \qquad (20)$$

where $\overline{v}$ is the time-mean velocity and v' is the departure from the time mean velocity. Multiply and expand:

$$H_q = \rho c_p \int_0^L \int_{-D}^0 (\overline{v} + v')(\overline{T} + T') dz dx \qquad (21a)$$

$$H_q = \rho c_p \int_0^L \int_{-D}^0 (\overline{vT} + \overline{v}T' + v'\overline{T} + v'T') dz dx \qquad (21b)$$

To determine the relative contributions of temperature variations and velocity variations, the magnitude of variations in the $\overline{v}T'$, $v'\overline{T}$, and $v'T'$ terms are plotted and compared. The $\overline{vT}$ term is ignored because it does not vary.

Because the noise in the mass budget is large compared to freshwater fluxes, freshwater transports are more difficult to calculate than salt transports (Ganachaud and Wunsch, 2003). Freshwater transports are therefore estimated from their relationship to the more easily calculated salt transports. In fact, a virtual salt flux is employed in the model used in the state estimate. Salt transports are calculated in the same manner as temperature transports except that they dimensionless; however, the salt transport is closely identified with the mass of salt that crosses a section in kg/s.

Freshwater transports can be inferred from salt transports by solving for the amount of freshwater that would have to be added to produce the same change in the salt to water ratio as the removal of a given amount of salt. The initial ratio of salt mass, s_0, to freshwater mass, h_0, is

$$\xi = \frac{s_0}{h_0}. \tag{22}$$

If a small amount of salt, Δs, is added, the ratio becomes

$$\xi_2' = \frac{s_0 + \Delta s}{h_0}. \tag{23}$$

Similarly, if the freshwater content is changed by a small quantity, Δh, with $|\Delta h| << h_0$, the ratio becomes

$$\xi_1' = \frac{s_0}{h_0 + \Delta h}. \tag{24}$$

In order for ξ_1' to equal ξ_2', the relation

$$\Delta h \approx -\frac{h_0 \Delta s}{s_0} \tag{25}$$

must be approximately true. This relation is applied to salt transports in the form

$$F_w = -\frac{F_s}{\xi_0}, \tag{26}$$

where

$$\xi_0 = \frac{s_0}{h_0} \approx 0.035 \tag{27}$$

is a ratio of salt mass to water mass typical of the ocean. From (26) and (27), the salt transport is

$$F_s = \sum_{i,k} S_{ik} v_{ik} \Delta x_i \Delta z_k. \tag{28}$$

Power density spectra of the transport time series are calculated. The Fourier series is calculated after subtracting the mean. Then the values are squared and sets of three consecutive values are averaged. These values are multiplied by half the number of data points in the original time series, and the resulting power density spectrum is plotted.

All uncertainties in calculated variables are estimated by the time standard deviation of the quantity as calculated from the monthly averaged data set. When transports are summed to find the net flux into or out of a region, the standard deviation reported is the square root of the sum of the variances of the transports.

4. Results

4.1 Time Mean Flow Characteristics

Across sections representing the only communication between a basin and the rest of the ocean, the time mean net volume transport must be nearly zero, except for small evaporation and precipitation terms. This is the case in all four Atlantic sections, the northernmost two Pacific sections and the zonal Southern Ocean section, and, indeed, the transports across these sections are indistinguishable from zero within their uncertainties. The transports across all sections and uncertainties as estimated by their standard deviations are shown in Table 1. Figure 3 shows the location of several of the sections on a map along with their mean transports. In the sections that do have net transports, two main patterns appear; one is an anticyclonic circulation around Australia, with a mean strength of approximately 11.3Sv, and the other is the eastward circulation of the Antarctic Circumpolar Current (ACC), with an approximate mean strength of 146±5Sv. An ACC of 146Sv is significantly larger than the Stammer et al. (2003) estimate of 124Sv.

Figure 3. Map showing time mean volume transports across zonal and meridional sections. The sections marked with zeros have mean volume transports smaller than their standard deviations.

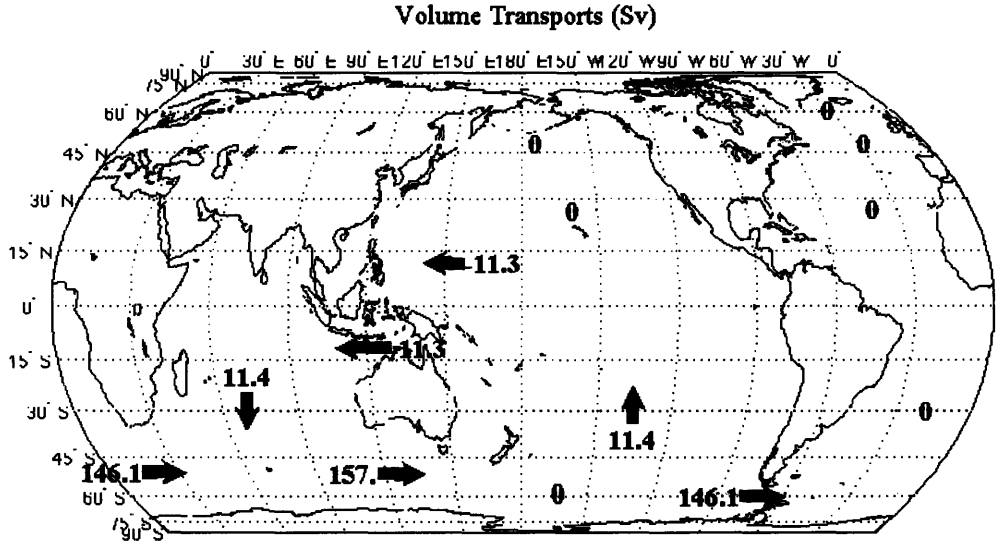

The 146Sv estimate is consistent with Nowlin and Klinck's (1986) estimate of 136±5Sv and Ganachaud and Wunsch's (2000) estimate of 140±7Sv cited in Stammer et al. (2003).

The mean ITF volume transport of approximately 11Sv is consistent with Stammer et al. (2003). The mean volume budget calculated from the assimilation is consistent with the fact that volume transported in the ITF must return to the Pacific; the ACC is stronger in the section south of Australia than in the other two meridional Southern Ocean sections by an amount equal to the volume transported in the ITF. Figure 8d shows that the strongest southward flow across 30°S in the Indian Ocean is concentrated near the western boundary. This is consistent with a strong southward current through the Mozambique Channel as described by Stammer et al. (2003). In fact, the flow is concentrated at the Western side of the Mozambique Channel as shown in Figure 8g, and the mean volume transport is 15.1±4.1Sv to the South, shown in Table 1. The transport of 15±4Sv through the Mozambique Channel is consistent with Stammer et al.'s (2003) estimate of 16Sv. There appears to be a slight inconsistency between the average of 11.4Sv transported across the 30°S Indian and Pacific Ocean sections and the 11.3Sv ITF, but the numbers are consistent within the standard deviations of their time variations, and the difference is likely due to rounding errors.

Table 1. Volume Transports. Eastward and northward transports are positive.

Section	Volume Transports
Atlantic 60N	-0.003 ± 0.083 Sv
Atlantic 48N	-0.003 ± 0.105 Sv
Atlantic 26N	0.004 ± 0.210 Sv
Atlantic 30S	0.002 ± 0.307 Sv
Pacific 48N	-0.001 ± 0.068 Sv
Pacific 26N	-0.003 ± 0.264 Sv
Pacific 30S	11.39 ± 2.63 Sv
Indian 30S	-11.40 ± 2.50 Sv
Southern 58S	-0.004 ± 0.188 Sv
Indonesia 114E	-11.34 ± 2.46 Sv
Indonesia 125E	-11.34 ± 2.45 Sv
Indonesia 153E	-11.34 ± 2.51 Sv
Southern 20E	146.14 ± 4.81 Sv
Southern 125E	157.47 ± 6.11 Sv
Southern 73W	146.14 ± 4.85 Sv
Mozambique Channel 20S	-15.12 ± 4.06 Sv
Luzon- China 121E	-1.09 ± 2.67 Sv
Sumatera - Borneo 1N	-1.98 ± 2.92 Sv
Borneo - Sulawesi 1S	-6.64 ± 3.41 Sv
Sulawesi - New Guinea 2S	-2.73 ± 2.54 Sv
Borneo - Mindanao 7N	0.89 ± 1.00 Sv

Since the net transport across 20°E and 73°W are both approximately 146Sv, it seems likely that that is representative of the strength

of the ACC. The mean eastward transport of 157.5Sv between Antarctica and Australia is equal to the sum of the ITF and the ACC, preserving the mass balance.

The state estimate mean flow successfully represents many currents, which can be identified in velocity contours across several of the sections. As Wunsch and Heimbach (2006) mentioned, a Gulf Stream, Antilles current, and deep western boundary current are present in the 26°N velocity section. The North Atlantic Current and Labrador Current are in Figure 7f. The velocity of the Labrador Current at 48°N is approximately 11cm/s southward. It transports approximately 1.6±1.0Sv to the south between 51°W and 45°W above 185m depth. The Brazil Current can be seen in Figure 7d.

The Oya Shio is present in Figure 8b, with a velocity of about 5cm/s southward and a transport of 11.6±3.7Sv at 48°N between 155°E and 166°E above 1750m. The Kuroshio can be identified in Figure 8a with a velocity of approximately 20cm/s northward, and between approximately 35°N and 40°N in Figure 10a. The Kuroshio transports 48.3±3.2Sv northward at 26°N between 121°E and 134°E above 1750m depth. Figure 8e has the East Australia Current, which has a strength of approximately 18cm/s and transports 22.9±2.6Sv southward between 154°E and 158°E at 30°S above 2200m depth. The Equatorial Countercurrent, North Equatorial Current, and South Equatorial Current can be identified in Figure 8i. The South Equatorial Current transports 21.9±10.9Sv westward at 140°W between 20°S and 3°S above 360m depth. The North Equatorial Current transports 18.9±2.7Sv westward at 140°W between 11°N and 27°N above 360m depth. The Equatorial Countercurrent transports 14.8±5.4Sv eastward at 140°W between 2°S and 10°N above 360m depth. In the 140°W section in Figure 8i the ACC is observed between about 50°S and 60°S.

The Mozambique Current is present in Figure 8d and g with a strength of 24cm/s and transports 15.1±4.1Sv southward. A westward Agulhas Current with a maximum strength of about 10 cm/s is visible in Figure 11b just south of the African coast in the Southern Ocean, and it is likely that at least some of the ITF water that passes through the Mozambique Channel continues on through the Agulhas into the Atlantic. The Agulhas Current transports approximately 21.5±2.7Sv westward across 20°E between 41°S and 35°S and above 2200m depth.

Figure 4. Map showing time mean atmospheric heat fluxes into ocean sections calculated as the sum of temperature transports out of the regions.

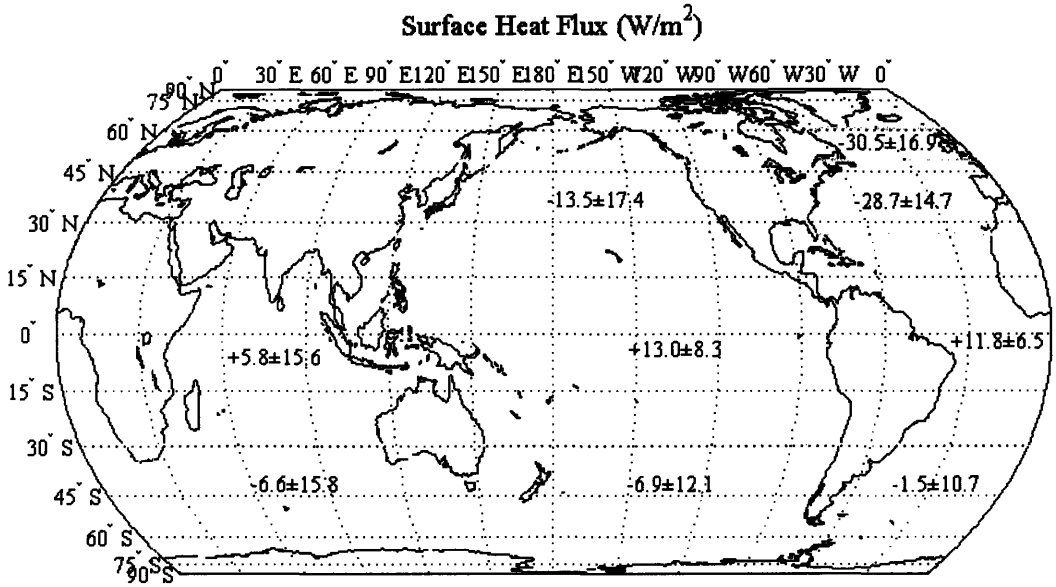

Figure 5. Time mean freshwater flux.

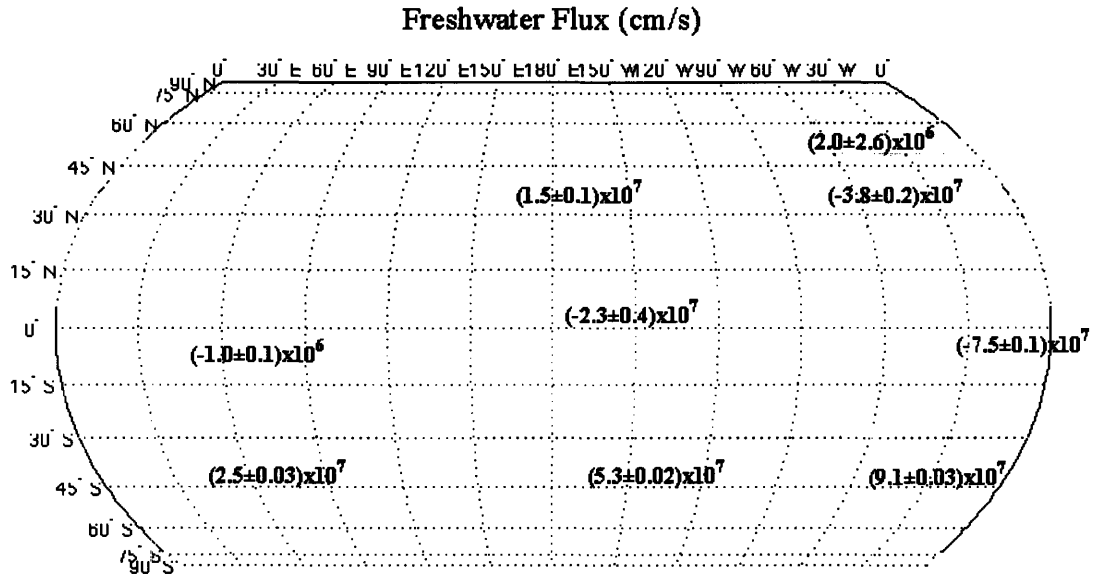

Table 2. Temperature transports and heat fluxes.

Section	Temperature Transport			
Atlantic 60N	0.289	±	0.037	PW
Atlantic 48N	0.453	±	0.083	PW
Atlantic 26N	0.837	±	0.179	PW
Atlantic 30S	0.354	±	0.196	PW
Pacific 48N	0.064	±	0.098	PW
Pacific 26N	0.393	±	0.414	PW
Pacific 30S	0.231	±	0.471	PW
Indian 30S	-1.085	±	0.326	PW
Southern 58S	-0.006	±	0.147	PW
Indonesia 114E	-0.906	±	0.358	PW
Indonesia 125E	-0.892	±	0.253	PW
Indonesia 153E	-1.077	±	1.228	PW
Southern 20E	1.149	±	0.107	PW
Southern 125E	2.065	±	0.206	PW
Southern 73W	1.536	±	0.089	PW
Mozambique Channel 20°S	-0.882	±	0.219	PW
Luzon- China 121E	-0.070	±	0.263	PW
Sumatera - Borneo 1N	-0.230	±	0.344	PW
Borneo - Sulawesi 1S	-0.460	±	0.320	PW
Sulawesi - New Guinea 2S	-0.162	±	0.303	PW
Borneo - Mindanao 7N	0.103	±	0.124	PW

Area	Net Temperature Transport	Heat Flux
Region 1	-0.164 ± 0.091 PW	-30.5 ± 16.9 W/m^2
Region 2	-0.384 ± 0.197 PW	-28.7 ± 14.7 W/m^2
Region 3	0.483 ± 0.266 PW	11.8 ± 6.5 W/m^2
Region 4	-0.033 ± 0.241 PW	-1.5 ± 10.7 W/m^2
Region 5	-0.329 ± 0.425 PW	-13.5 ± 17.4 W/m^2
Region 6	1.053 ± 0.676 PW	13.0 ± 8.3 W/m^2
Region 7	-0.298 ± 0.522 PW	-6.9 ± 12.1 W/m^2
Region 8	0.179 ± 0.484 PW	5.8 ± 15.6 W/m^2
Region 9	-0.168 ± 0.401 PW	-6.6 ± 15.8 W/m^2

Figure 6. Map identifying regions by number.

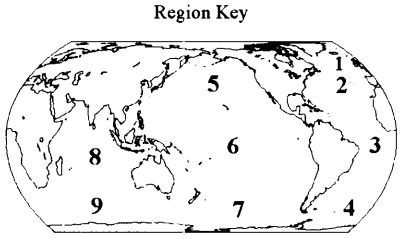

Figure 4 shows the net heat fluxes from atmosphere to ocean in regions bounded by sections along which temperature transports are calculated. The heat fluxes are calculated by summing the total oceanic heat transport out of the region. The map clearly shows that the ocean gains heat near the equator and gives off heat near the poles.

Time mean temperature transports across each of the sections, as well as the heat fluxes into several regions, are shown in Table 2. The regions are defined in Figure 6. The ITF transports approximately 0.9PW to the Indian Ocean, on average. This value is slightly less than that of Stammer et al. (2003), but the error bounds of the two estimates overlap. The transport of 0.46±0.32PW through the Makassar Strait between Borneo

and Sulawesi is consistent with Vranes et al.'s (2002) estimate of 0.5PW. Of the North Atlantic sections, the one with the greatest average northward heat flux is the 26°N section, at 0.84±0.18PW. The mean heat flux across the 30°S Atlantic section is directed toward the equator. This was also the case in the Ganachaud and Wunsch (2003) study. The mean Pacific meridional heat flux is much smaller than that of the Atlantic, with a value of 0.39±0.41PW northward at 26°N, which is indistinguishable from zero relative to its error.

At 48°N, the mean thermocline depth slopes downward from West to East in both the Atlantic and the Pacific, although the slope in the Atlantic is greater. In general, poleward flowing currents are associated with dips in isotherms as they bring warm water into cold regions, and currents flowing toward the equator are associated with isotherms protruding upward as they bring cold water into warm regions. In many cases, mean temperature and salinity fields have similar features. For example compare Figure 7b and Figure 7c or Figure 11f and Figure 11g. The similarity is most striking in the Atlantic.

The uncertainties of many of the mean freshwater transports based on their standard deviations are larger than the estimates themselves. However, the freshwater transports in Regions 2, 3, and 6 are consistent with transports in similar regions studied by Ganachaud and Wunsch (2003). In Figure 5, a map of freshwater fluxes into enclosed regions, the mean freshwater flux is generally negative into equatorial regions and positive into high-latitude regions. This indicates equatorial evaporation and precipitation at higher latitudes. However, as previously mentioned, the values are all smaller than their estimated uncertainties. Freshwater transports are listed in Table 3.

The salinity contours at 30°S and 26°N, for example in Figure 8f, all have higher salinity at the surface consistent with evaporation. The Southern Ocean, in contrast, seems to have lower salinity at the surface than at depth, as does the Pacific at 48°N. The Atlantic, however, has higher salinity near the surface at 48°N.

Table 3. Freshwater transports and fluxes.

Section	Freshwater Transport
Atlantic 60N	1.41E+08 ± 0.85E+08 kg/s
Atlantic 48N	2.51E+08 ± 1.09E+08 kg/s
Atlantic 26N	2.00E+08 ± 2.31E+08 kg/s
Atlantic 30S	-1.09E+08 ± 3.48E+08 kg/s
Pacific 48N	1.15E+08 ± 1.41E+08 kg/s
Pacific 26N	1.51E+08 ± 2.96E+08 kg/s
Pacific 30S	1.11E+10 ± 0.26E+10 kg/s
Indian 30S	-1.15E+10 ± 0.25E+10 kg/s
Southern 58S	-3.89E+08 ± 2.24E+08 kg/s
Indonesia 114E	-1.12E+10 ± 0.24E+10 kg/s
Indonesia 125E	-1.11E+10 ± 0.24E+10 kg/s
Indonesia 153E	-1.15E+10 ± 0.25E+10 kg/s
Southern 20E	1.44E+11 ± 0.05E+11 kg/s
Southern 125E	1.55E+11 ± 0.06E+11 kg/s
Southern 73W	1.44E+11 ± 0.05E+11 kg/s
Mozambique Channel 20°S	-1.51E+10 ± 0.41E+10 kg/s
Luzon- China 121E	-1.10E+09 ± 2.62E+09 kg/s
Sumatera - Borneo 1N	-1.87E+09 ± 2.77E+09 kg/s
Borneo - Sulawesi 1S	-6.57E+09 ± 3.34E+09 kg/s
Sulawesi - New Guinea 2S	-2.72E+09 ± 2.48E+09 kg/s
Borneo - Mindanao 7N	8.69E+08 ± 9.79E+08 kg/s

Area	Net Freshwater Transport	Approximate Freshwater Flux
Region 1	1.1E+08 ± 1.4E+08 kg/s	2.0E-06 ± 2.6E-06 cm/s
Region 2	-5.1E+07 ± 2.6E+08 kg/s	-3.8E-07 ± 1.9E-06 cm/s
Region 3	-3.1E+08 ± 4.2E+08 kg/s	-7.5E-07 ± 1.0E-06 cm/s
Region 4	2.0E+08 ± 6.8E+09 kg/s	9.1E-07 ± 3.0E-05 cm/s
Region 5	3.6E+07 ± 3.3E+08 kg/s	1.5E-07 ± 1.3E-06 cm/s
Region 6	-1.9E+08 ± 3.6E+09 kg/s	-2.3E-07 ± 4.4E-06 cm/s
Region 7	2.3E+08 ± 8.2E+09 kg/s	5.3E-07 ± 1.9E-05 cm/s
Region 8	-3.2E+08 ± 3.4E+09 kg/s	-1.0E-06 ± 1.1E-05 cm/s
Region 9	6.3E+07 ± 8.1E+09 kg/s	2.5E-07 ± 3.2E-05 cm/s

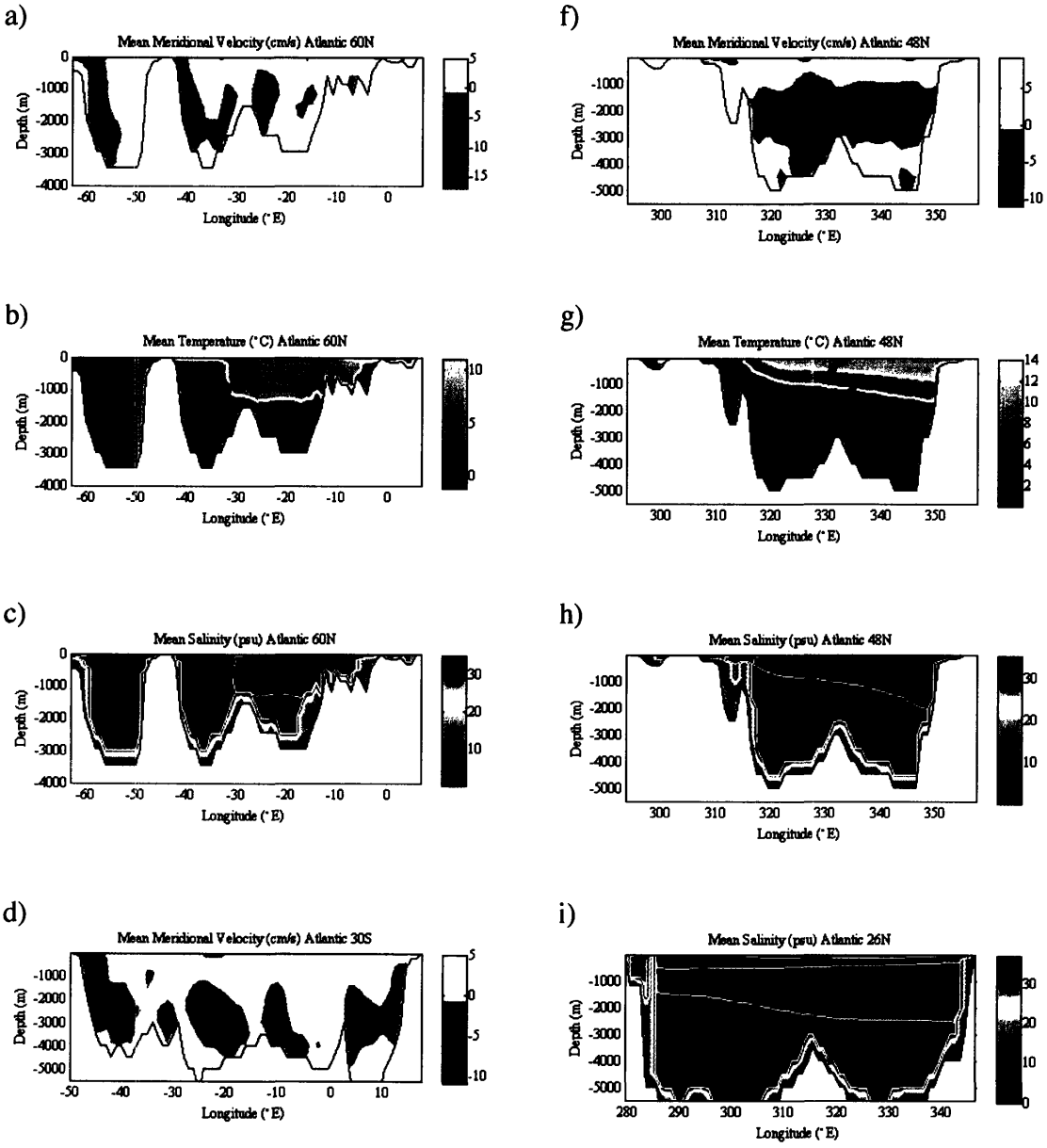

Figure 7. Atlantic section contours. a) Velocity across 60°N. b) 60°N temperature profile. c) 60°N salinity profile. d) Velocity across 30°S. e) 30°S salinity profile. f) Velocity across 48°N. g) 48°N temperature profile. h) 48°N salinity profile. i) 26°N salinity profile.

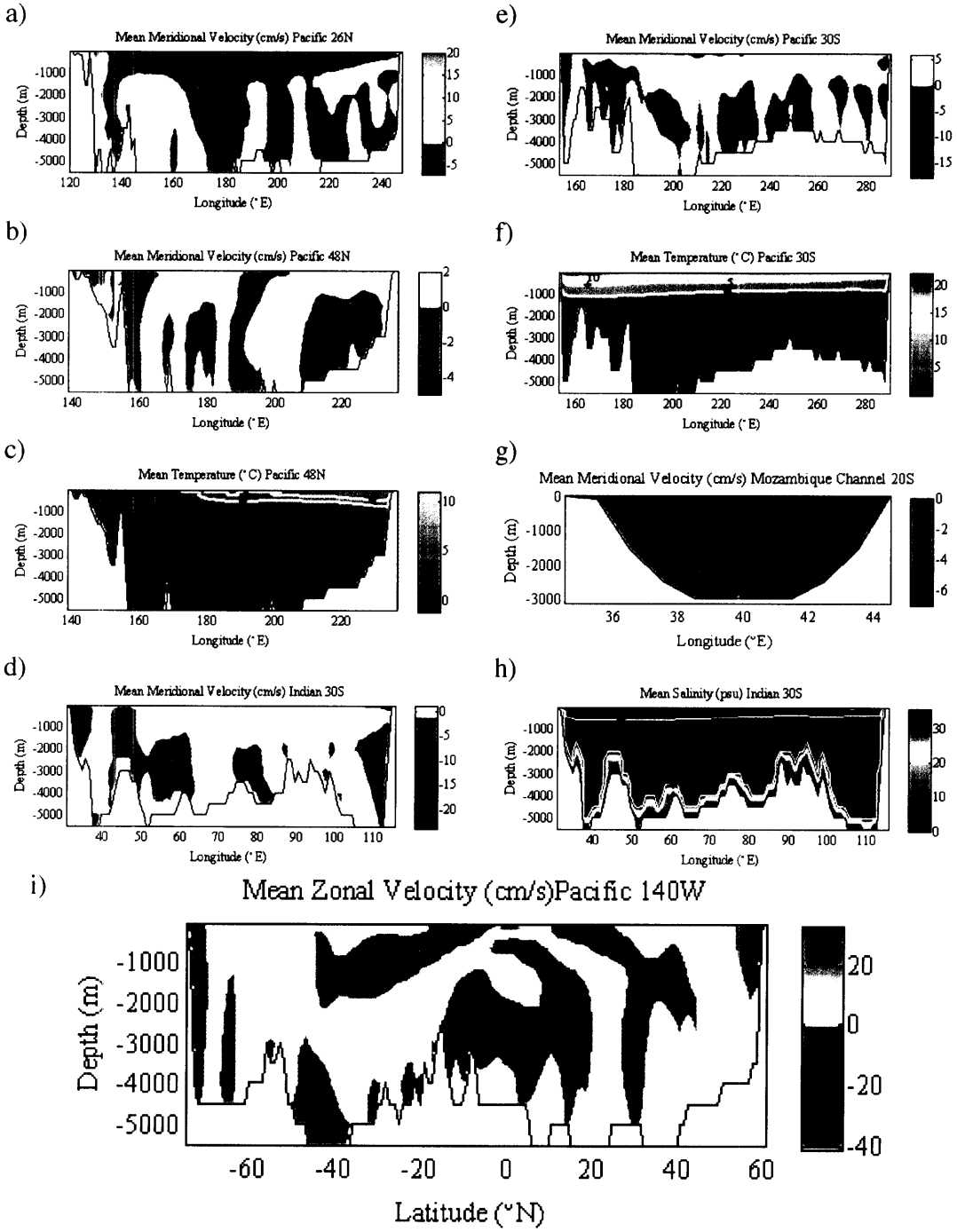

Figure 8. Pacific and Indian Ocean section contours. a) Velocity across 26°N. b) velocity across 48°N. c) 48°N temperature profile. d) Velocity across 30°S Indian Ocean. e) Velocity across 30°S Pacific. f) 30°S Pacific temperature profile. g) Velocity across 20°S in the Mozambique Channel. h) 30°S Indian Ocean salinity profile. i) Velocity across 140°W Pacific.

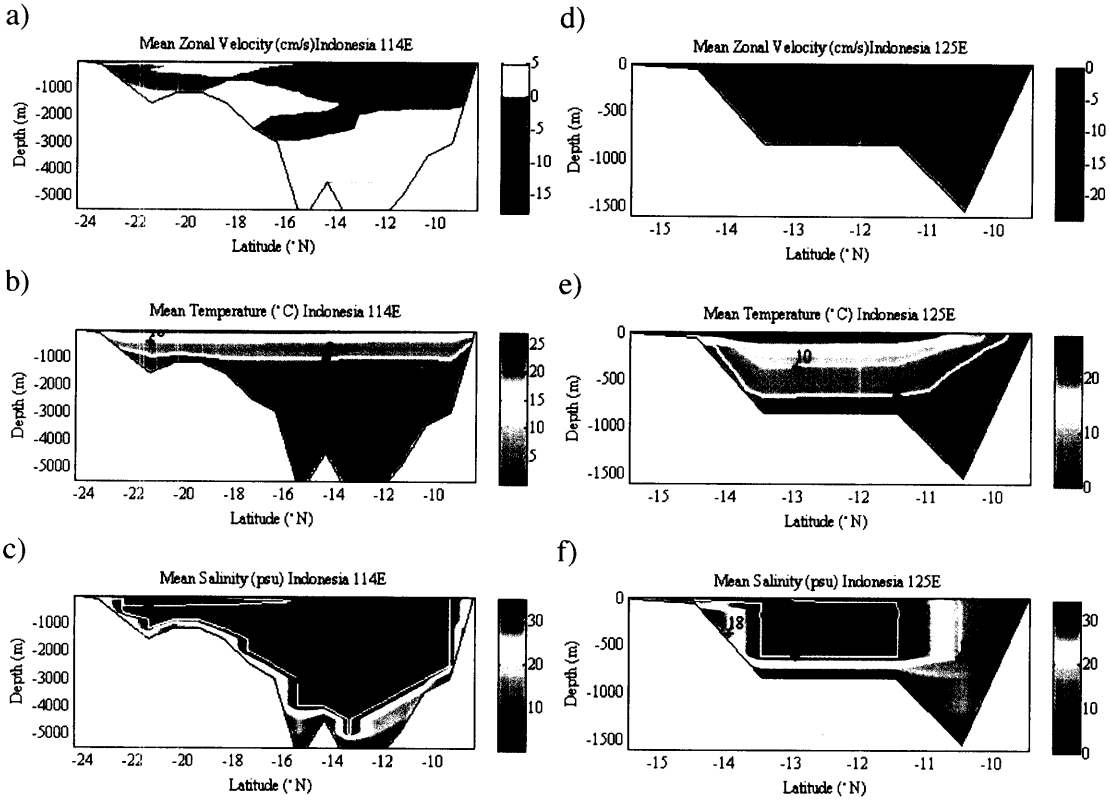

Figure 9. Contours of Indonesian Throughflow. a) Velocity across 114°E. b) 114°E temperature profile. c) 114°E salinity profile. d) Velocity across 125°E. e) 125°E temperature profile. f) 125°E salinity profile.

a)

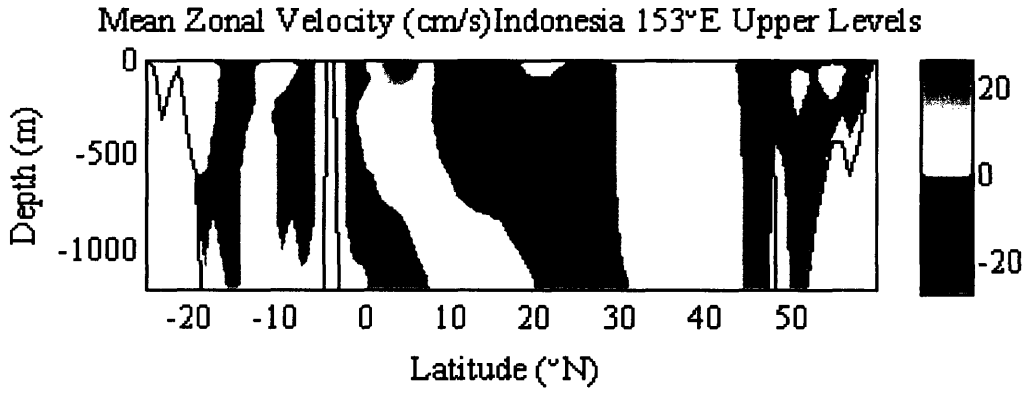

b)

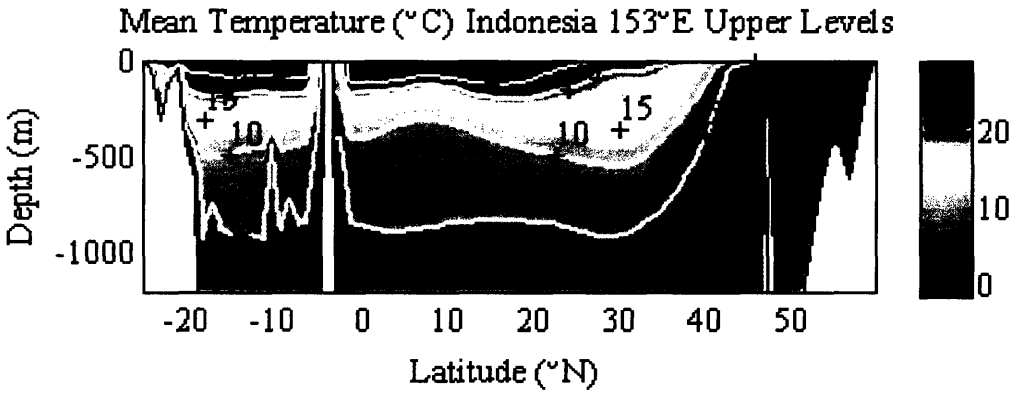

c)

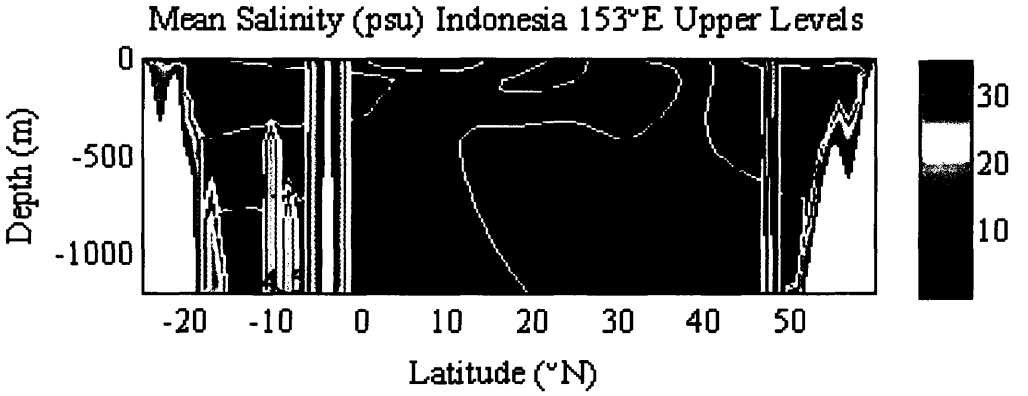

Figure 10. 153°E Western Pacific/Indonesian region contours. a) Velocity across 153°E. b) Temperature profile. c) Salinity profile.

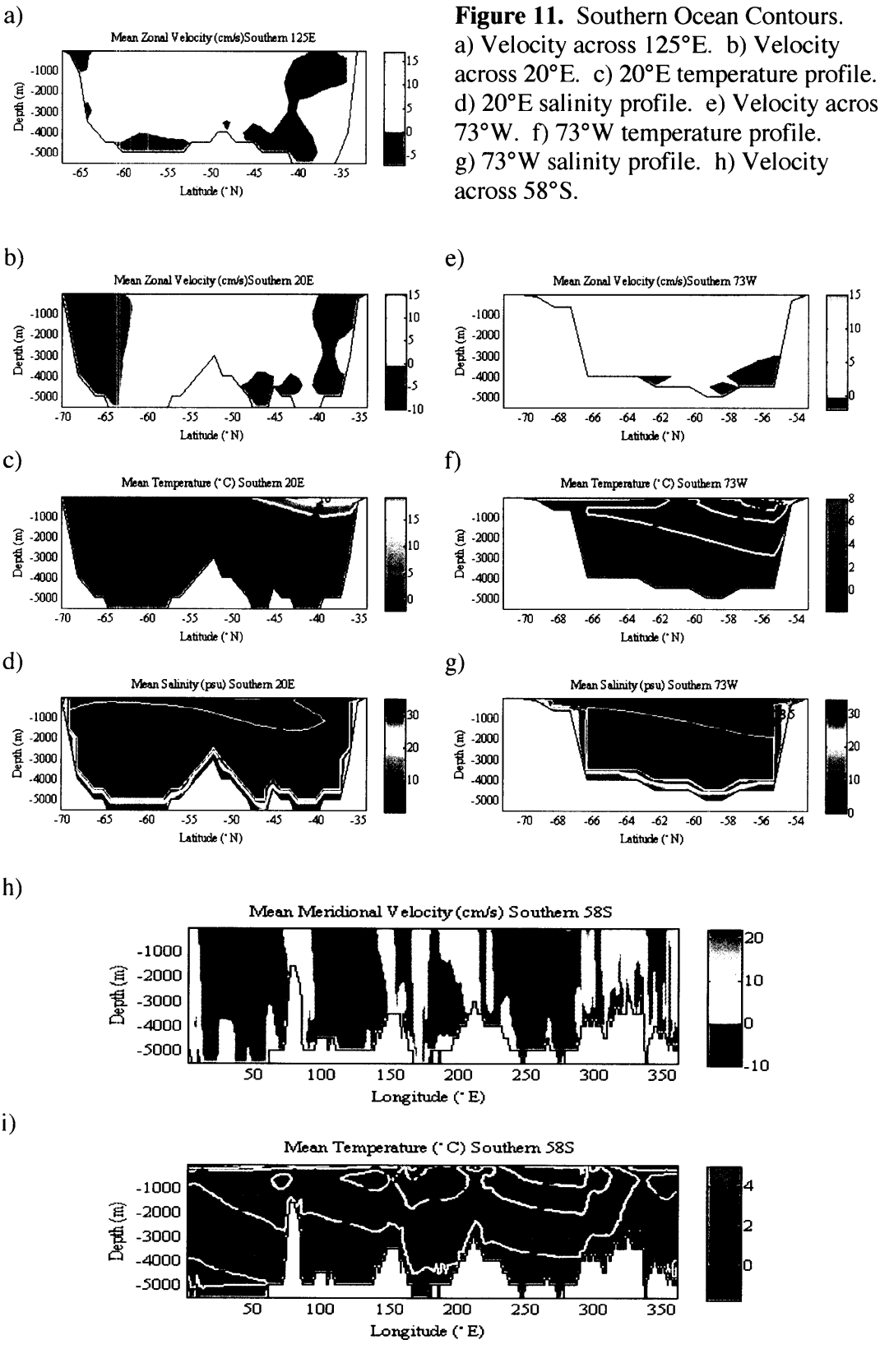

Figure 11. Southern Ocean Contours. a) Velocity across 125°E. b) Velocity across 20°E. c) 20°E temperature profile. d) 20°E salinity profile. e) Velocity across 73°W. f) 73°W temperature profile. g) 73°W salinity profile. h) Velocity across 58°S.

4.2 Variability

Typical plots of transports vs. time are shown in Figure 12. Most of the sections analyzed here have time series similar to Figure 12, with many fluctuations at various frequencies about a mean value. Annual cycles are prominent in many of the volume, temperature, and salt transport records. One such cycle can be discerned from the contour plot of volume transport against depth and time in Figure 14; between about 1000m and 2000m depth, there is a seasonal cycle in which the net zonal volume transport across the section changes sign.

Most of the power densities have strong peaks at the annual cycle of 1/12 months^{-1}. The power density plots in Figure 13a are typical of the 26°N and 30°S meridional transport plots as well as the ITF and Southern Ocean zonal transport plots. The plots have a spike at the annual frequency and little energy elsewhere. The 48N and 60N sections tend to have more power at higher frequencies than the 26N and 30S power density plots. For example, Figure 13b shows that at 48°N in the Atlantic there is little power at the annual cycle in temperature and salt transport records but more power at

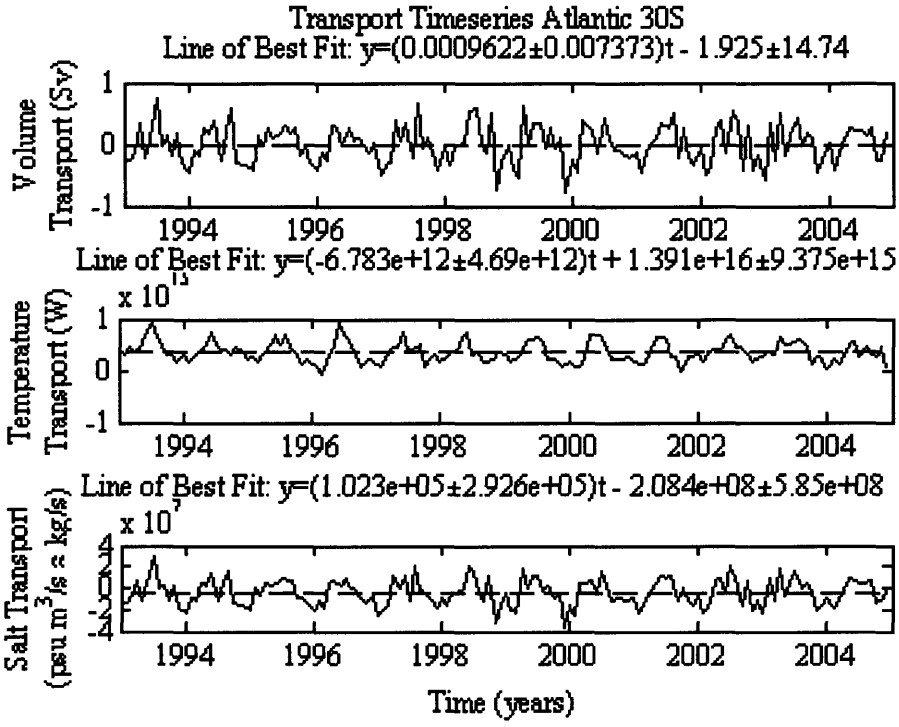

Figure 12. Atlantic 30°S transport time series and line of best fit.

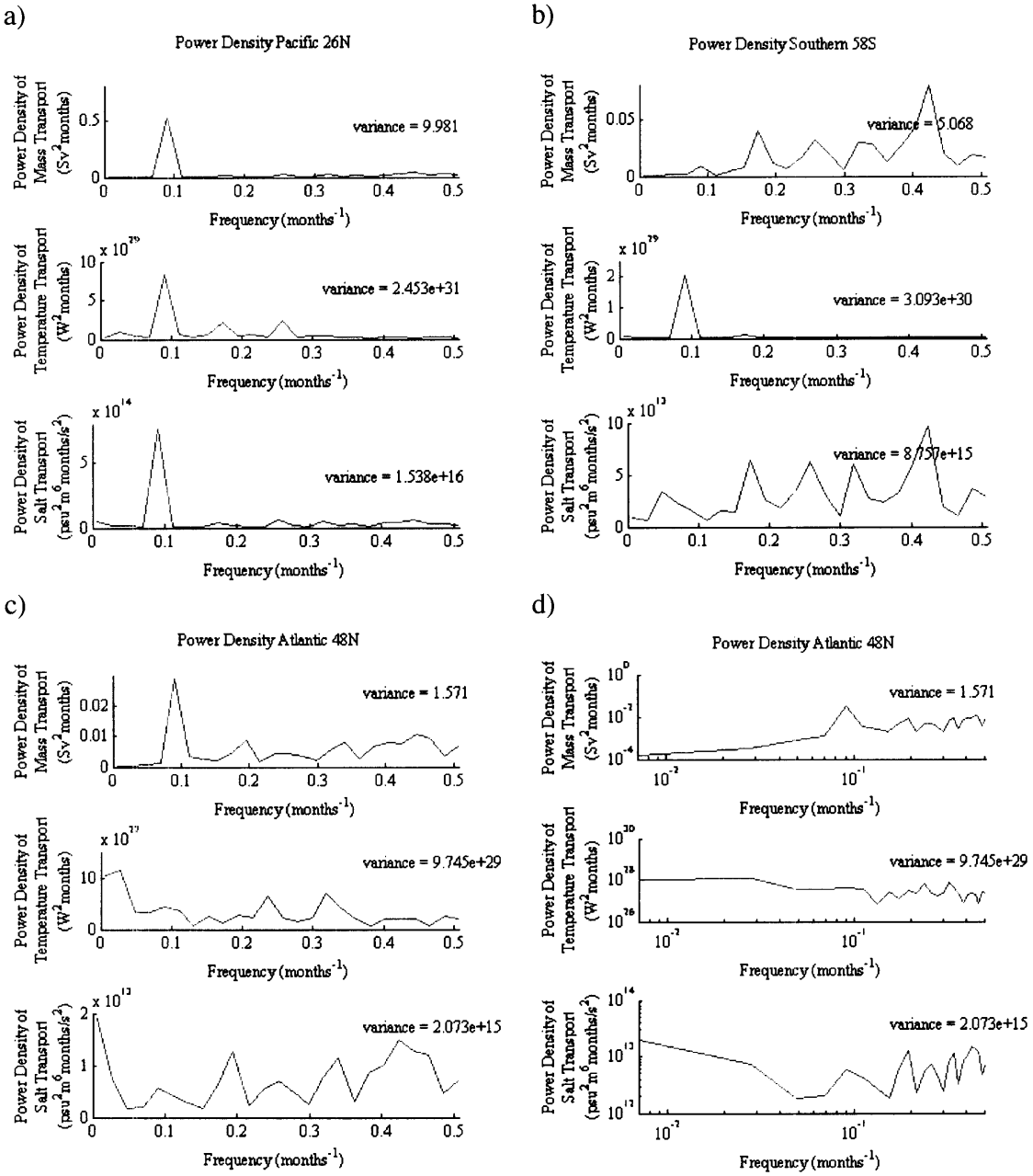

Figure 13. Power density spectra. a) 26°N Pacific, linear axes. b) 58°S Southern Ocean, linear axes. c) 48°N Atlantic, linear axes. d) 48°N Atlantic, log-log plot. Linear axes are used because there is little information at low frequencies (compare c and d).

higher frequencies. Figure 13c shows that the meridional volume transport across 58°S also has significant power at higher frequencies, while the temperature transport has almost all of its power at the annual cycle.

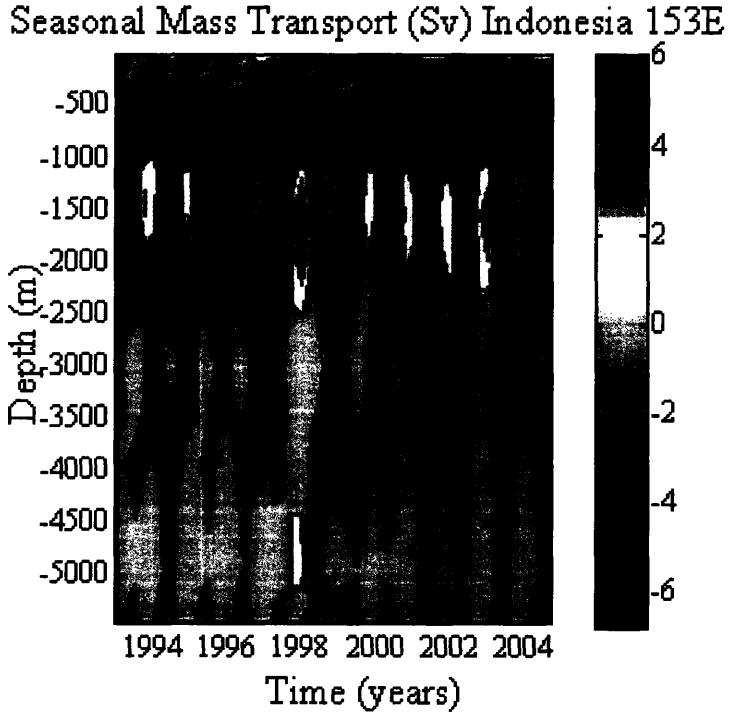

Figure 14. Contour plot of transports vs. depth and time at 153°E, filtered to show seasonal variability.

The route of the Indonesian throughflow varies seasonally. Figure 16 is a plot of the monthly mean volume transports across several sections in the Indonesian region. Figure 15 shows the mean flow across various sections in the Indonesian region in December, January, February (boreal winter), and June, July, August (boreal summer). The ITF is stronger in boreal summer than boreal winter, with a mean summer transport of 13.2±1.5Sv and a mean winter transport of 8.8±1.7Sv at 153°E. This is consistent with Meyers et al.'s (1995) observation that the ITF was strongest from July to September. In boreal summer, flows actually reverse in the passages between Luzon and China, with a flow of 1.6±0.9Sv eastward, and between Sumatera and Borneo, with a flow of

1.2±0.7Sv northward. The transport though the Makassar Straight between Borneo and Sulawesi is much stronger in boreal summer with a southward flow of 10.2±1.6Sv compared to 2.7±1.7Sv in winter. The southward transport between Sulawesi and New Guinea is also stronger in boreal summer.

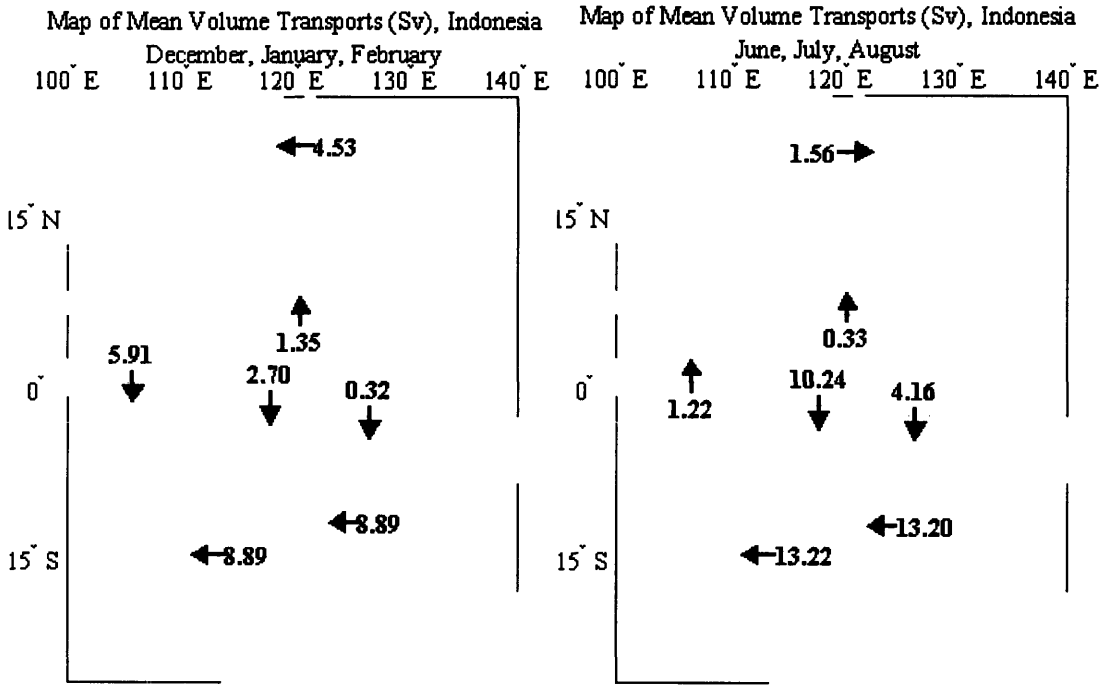

Figure 15. Seasonal differences in volume transports in the Indonesian Passages.

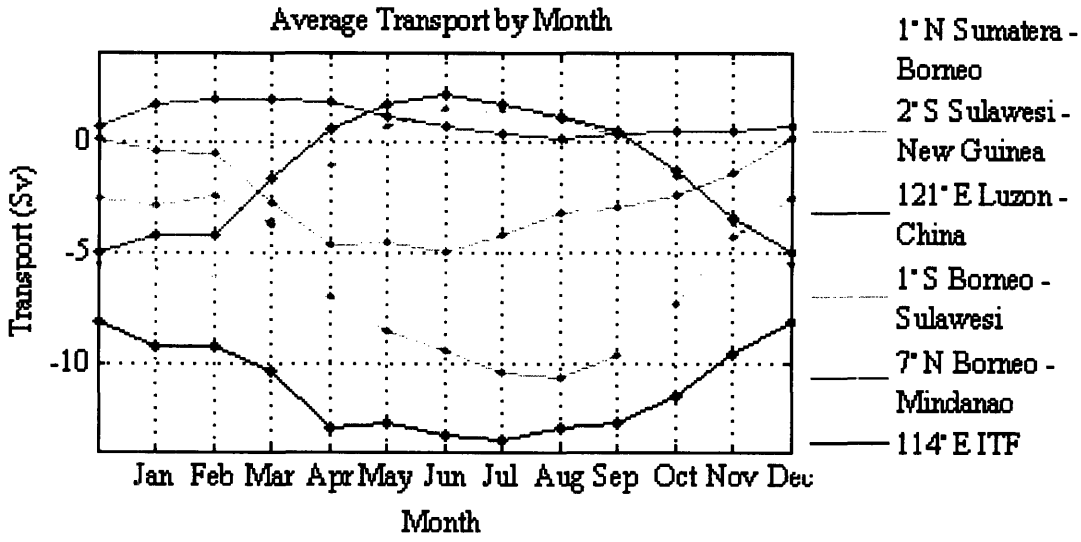

Figure 16. Monthly mean volume transport in several Indonesian passages.

a)

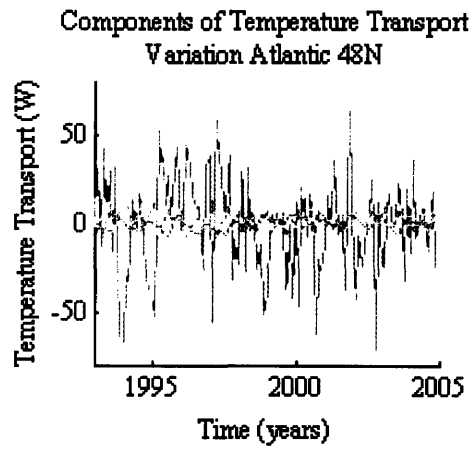

b)

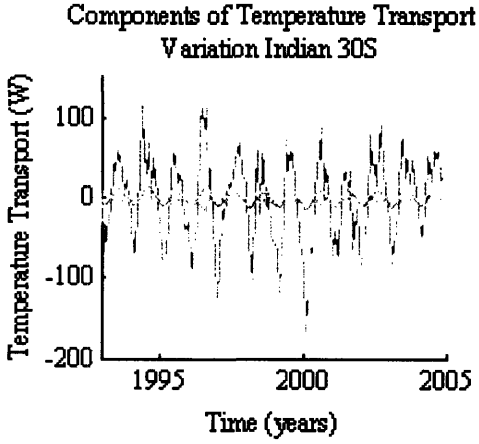

c)

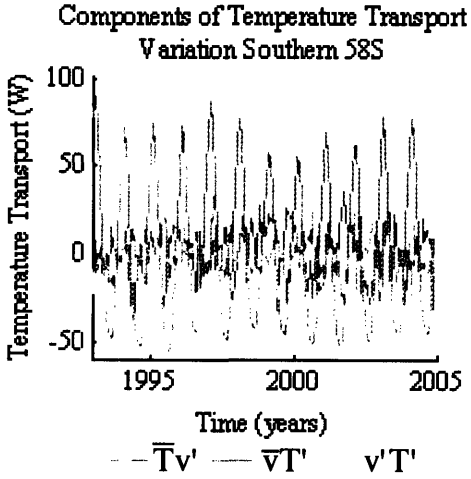

Figure 17. Components of temperature transport variation. a) 48°N Atlantic. b) 30°S Indian Ocean. c) 58°S Southern Ocean.

In order to assess the relative importance of variations in temperature and velocity to temperature transport fluctuations, the three terms of the variation are plotted together versus time. These terms are the products of mean temperature and velocity anomaly, mean velocity and temperature anomaly, and velocity anomaly and temperature anomaly. Three of these plots are shown in Figure 17a, b, and c.

In the Atlantic, $\overline{T}v'$ has the largest fluctuations at each section, as in Figure 17a. As the latitude becomes higher, $\overline{T}v'$ becomes slightly smaller, causing the $\overline{v}T'$ and $v'T'$ terms to become relatively more important. However, $\overline{T}v'$ remains by far the largest component, indicating that velocity fluctuations are responsible for most of the temperature transport variability in the Atlantic.

Velocity fluctuations also have more impact than temperature fluctuations on temperature transports in the ITF, the Indian Ocean at 30°S and the Mozambique Channel, and in the Pacific. The relative magnitudes of the components of temperature transport variability at 30°S in the Indian Ocean are evident in Figure 17b. In the North

Pacific, the $\overline{v}T'$ and $v'T'$ components become more relevant at 48°N, as in the Atlantic, while still remaining smaller than $\overline{T}v'$.

The only sections on which temperature variations are responsible for the largest fluctuations are 58°S and 73°W in the Southern Ocean. The 58°S comparison is shown in Figure 17c. On the 58°S and 73°W sections the $\overline{v}T'$ term has the largest magnitude fluctuations. In the other two Southern Ocean sections, 125°E and 20°E, the $\overline{v}T'$ term is almost as large as the $\overline{T}v'$ term, and the $v'T'$ term is quite small. While in most of the areas analyzed, velocity fluctuations are responsible for the largest part of the temperature transport variability, temperature fluctuations are more important in some parts of the Southern Ocean.

4.3 Trends and Vertical Structure

The interpretation of apparent trends in the model output is not necessarily straightforward. It can be difficult to distinguish real physical trends from drift due to model error or variability on timescales longer than the record length. Regardless of their origins, trends can be found in much of the model output.

The only trends found in the volume transport time series are decreasing the magnitude of the flow. They are found in the 30°S Pacific section, 30°S Indian Ocean section, 114°E, 125°E, and 153°E Indonesian sections, and the three meridional Southern Ocean sections. The circulation around Australia is decreasing by approximately 0.065Sv/year, while the ACC Circulation is decreasing by approximately 0.88Sv/year. The decreases in both circulations represent approximately 6% drops in their strengths over ten years. The volume transport time series at 73°W in the Southern Ocean, shown in Figure 18, shows a visible downward trend. Such a trend was observed by Stammer et al. (2003) in their previous state estimate.

Temperature transports are decreasing in magnitude at 60°N and 30°N in the Atlantic, 48°N in the Pacific, 114°E and 125°E in the Indonesian region, and 125°E and 73°W in the Southern Ocean, but increasing at 26°N in the Pacific. Salt transports, which are inversely related to freshwater transports, are increasing in magnitude at 48°N and 26°N in the Atlantic, and 48°N and 26°N in the Pacific, but decreasing at 30°S in the

Indian Ocean, 114°E and 125°E in the Indonesian region, and at all of the Southern Ocean meridional sections, likely due to the decrease in volume transport there.

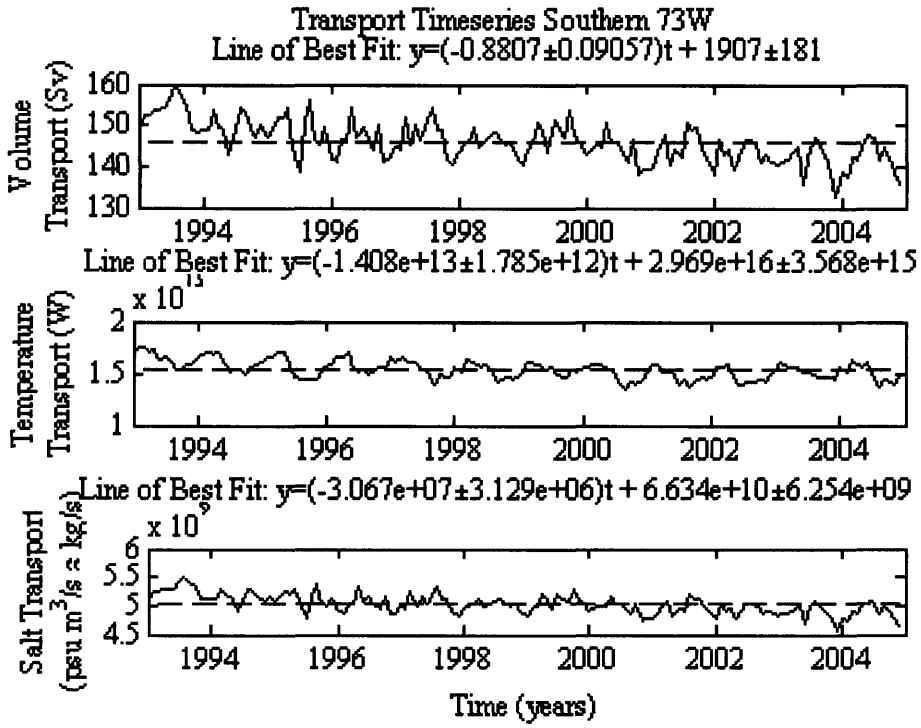

Figure 18. 73°W Southern Ocean transport time series and lines of best fit.

Many of the volume transport records show vertical structure that persists in time. Typically, in the Atlantic Ocean, there are three distinct regions of flow: an upper, northward flow, an intermediate southward flow that Wunsch and Heimbach (2006) identify with NADW, and an abyssal flow that is very small and often northward. The pattern of upper, intermediate, and abyssal flow can be seen for 48°N in the Atlantic in Figure 19. In transport time series divided into segments according to these flow patterns, as in Figure 20, the upper and middle segments of the volume and salt transports nearly mirror each other. This makes sense because volume is conserved and the salt transports are closely tied to the volume transports. However, the temperature transports are different; nearly all of the fluctuations in temperature transports as well as the largest magnitudes occur in the upper level. This also makes sense, because there are greater temperature variability and warmer temperatures near the surface.

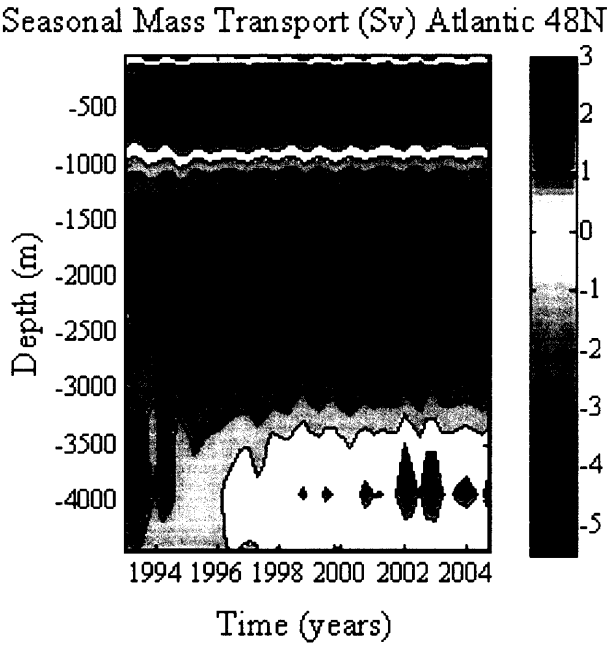

Figure 19. Contour plot of volume transport vs. depth and time, 48°N Atlantic, filtered to show seasonal variability.

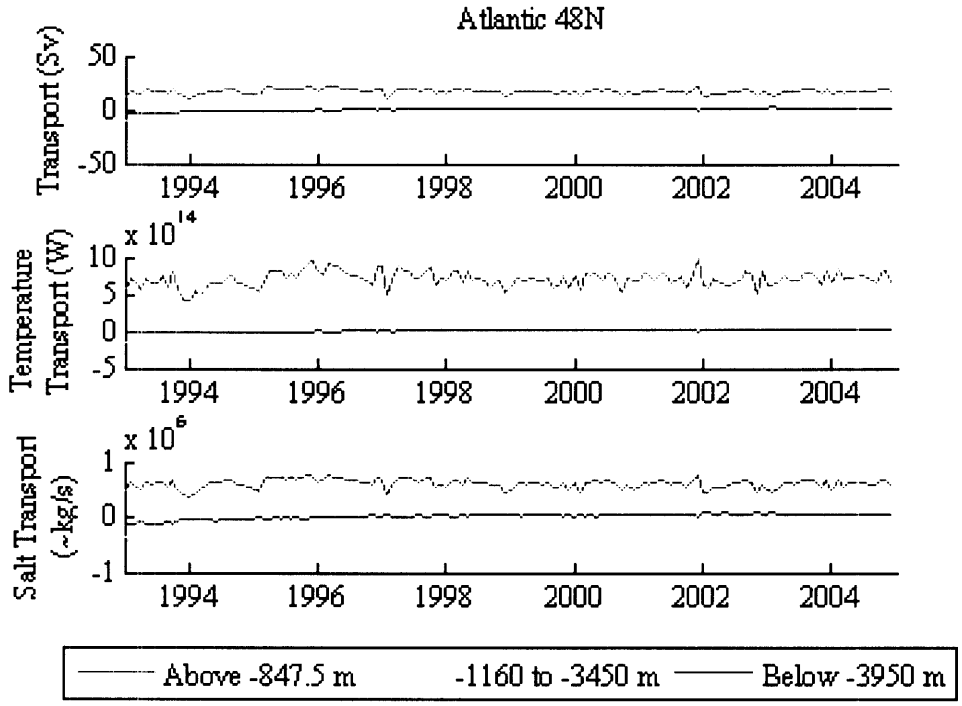

Figure 20. Components of transports separated by depth, 48°N Atlantic.

At 60°N in the Atlantic, the northward upper flow, southward intermediate flow, and northward bottom flow are all increasing in strength and temperature transport. However, as mentioned earlier, the net result is a slight decrease in temperature transport. At 48°N, the magnitude of the volume transport at 847m and above is decreasing slightly, but the magnitude of the volume transport at the intermediate and deep levels is increasing in magnitude. The temperature transports are increasing in magnitude at each level. The same is true at 26°N. There is no discernible trend in net volume transport or temperature transport at 48°N or 26°N. Figure 21a is a plot of volume transports versus depth and time at 30°S in the Atlantic. At 30°S in the Atlantic, the volume transport is decreasing in magnitude at all levels, and the temperature transport is decreasing in magnitude in the upper and intermediate zones but increasing below about 4000m. The result is a net decrease in temperature transport. It seems that the upper segment of the Atlantic's circulation may be decreasing in strength (except at 48°N), but deeper flows are strengthening (except at 30°S). At 48°N and 26°N, the upper level temperature transports are increasing despite the decreasing volume transport.

In the Pacific, the vertical structure of the volume transports is not as sharply delineated. At 30°S (Figure 21b) there appears to be some structure similar to that of the Atlantic, with northward upper flow, southward intermediate flow, and northward abyssal flow, but this structure is less apparent at 26°N and 48°N (Figure 21c). Plots of transports in different depth zones show that in the Pacific most of the heat transport occurs near the surface but the volume transports do not demonstrate nearly as well-defined a structure as in the Atlantic. At 30°S in the Indian Ocean (Figure 21d), the net volume transports are southward above about 2000m, and transition to northward between about 2000m and 4000m.

In the Southern Ocean, the maximum eastward transport occurs between about 500m and 1500m depth and tapers off toward the surface and toward the ocean floor. Figure 22 demonstrates the magnitude of the volume transport between 300m and 2500m. The largest decrease in volume transport occurs between about 300m and 2500m depth. Across the zonal section at 58°S, a fluctuating Northward flow occurs very close to the surface, in the upper 100m, and is balanced by a return flow below 2000m (Figure

23). Almost all of the meridional temperature transport occurs in the upper 100m, and there is a clear seasonal cycle. In the region between 100m and 1500m, the mean flow is only -1.84±0.38Sv, and there is very little variation. This region of small meridional volume transport and few fluctuations coincides with the depth of maximum eastward flow.

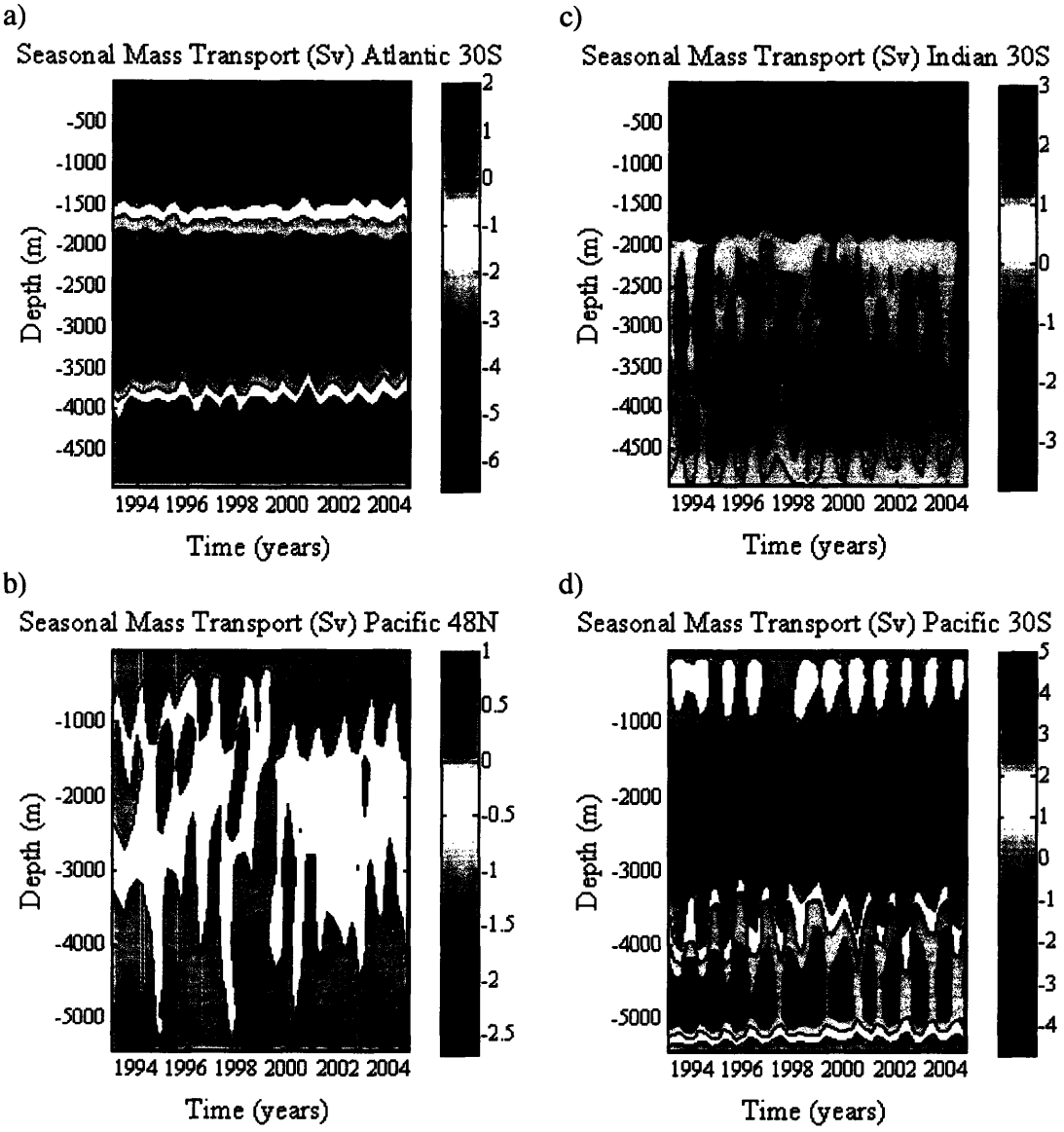

Figure 21. Contours of volume transport vs. depth and time, filtered to show seasonal variability. a) 30°S Atlantic. b) 48°N Pacific. c) 30°S Indian Ocean. d) 30°S Pacific.

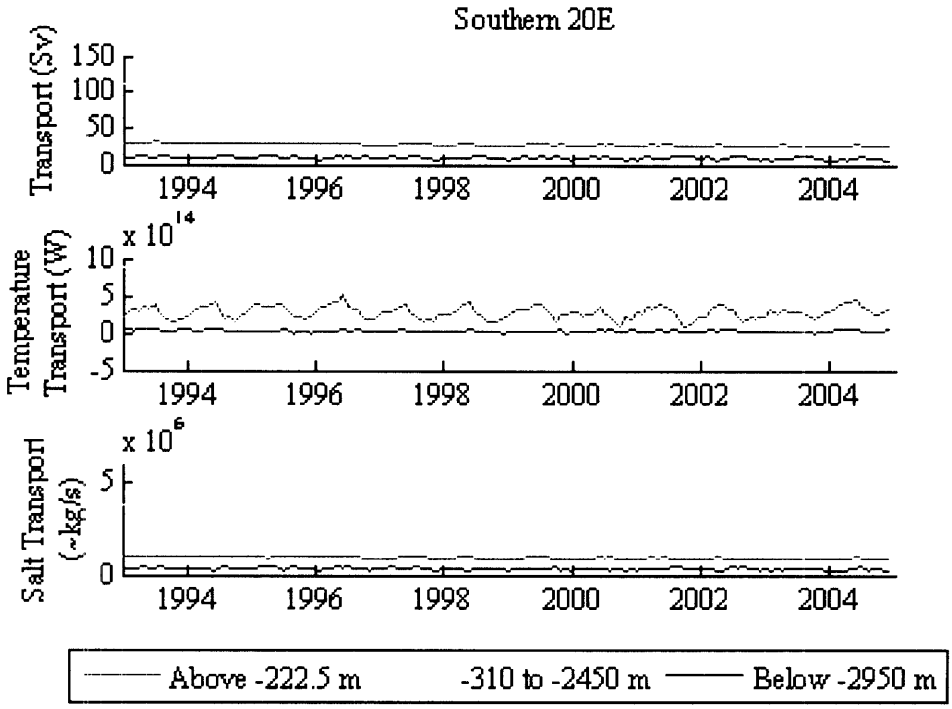

Figure 22. Components of transports separated by depth, 20°E Atlantic.

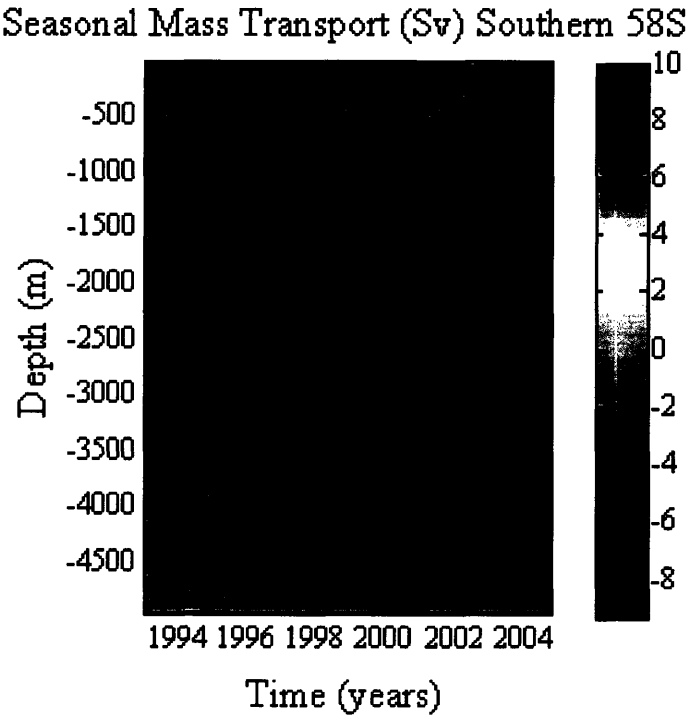

Figure 23. Contour of volume transport vs. depth and time, 58°S Southern Ocean, filtered to show seasonal variability.

5. Conclusions

Two advantages of this state estimate analysis over the Stammer et al. (2003) analysis are the extension of the time interval studied and the increased model resolution of one degree rather than two degrees. In general, the results agree qualitatively with those of Stammer et al. (2003), but there are some quantitative differences.

Time mean flow characteristics of the state estimate demonstrate overall agreement with previous estimates and known dynamics in many respects. The 146±5Sv strength of the ACC is larger than the Stammer et al. (2003) estimate of 124Sv but is within the range of other estimates. The ITF transport of 11Sv is also within the expected range. The ITF transport is stronger in boreal summer than boreal winter by approximately 4Sv. Time mean transports are indistinguishable from zero except in sections that cut through circulation loops such as the ACC and the circulation around Australia. Major currents are present in the mean flow, such as the Kuroshio, Oya Shio, and Gulf Stream. The model resolution is fine enough that the North Equatorial Current, South Equatorial Current, and Equatorial Countercurrent can all be identified.

In many sections, there is a strong peak in the power density spectra at the annual cycle. Higher frequency variability is also present in most sections. Most temperature transport variability results from velocity fluctuations, except in the Southern Ocean where temperature fluctuations are more important. Meridional temperature transport in the Southern Ocean is concentrated in a shallow layer near the surface.

A twelve-year decreasing trend is observed in the strength of the ACC of approximately 0.88Sv/year. There is also a decreasing trend in the strength of the ITF of 0.065Sv/year. Both trends represent approximately 6% decreases in the transport of the currents over ten years. Caution must be exercised in extrapolating these trends to future behavior as it is not clear whether the trends are the result of model drift, low frequency variability, or true shifts in ocean dynamics. Changes in upper level transports in the Atlantic often do not correspond to changes in the total transports, as lower level transports are changing as well.

Recommended future work includes studying seasonal variations in currents and transports in greater detail, analyzing vertical velocities, and looking for ENSO signals

and teleconnections. More sections could be added to the analysis. Of course, the state estimate itself continues to evolve as well.

Acknowledgements

I would like to thank my thesis advisor, Professor Wunsch, for his patience and guidance, especially for answering my many questions as I worked on this project. I would also like to thank Diana Spiegel for all of her programming tips and for helping me learn to use Linux. I would like to thank my parents for all their support and advice. Finally, I would like to thank the National Ocean Partnership Program for funding this work.

References

About CMI: MIT's Climate Modeling Initiative. <http://paoc.mit.edu/cmi/aboutcmi.htm> (1 August 2006).

Argo. 10 July 2006. <http://www.argo.ucsd.edu/> (1 August 2006).

Ganachaud, A., and C. Wunsch. 2002. Oceanic nutrient and oxygen transports and bounds on export production during the World Ocean Circulation Experiment. *Global Biochem. Cycles* 16: 1057.

Ganachaud, A. and C. Wunsch. 2003. Large-Scale Ocean Heat and Freshwater Transports during the World Ocean Circulation Experiment. *Journal of Climate* 16: 696-705.

Heimbach, P. and C. Evangelinos. *Estimating the Circulation and Climate of the Ocean.* 9 June 2006. <http://ecco.mit.edu/ecco/> (1 August 2006).

Marshall, J., A. Adcroft, C. Hill, L. Perelman, and C. Heisey. 1997. A finite-volume, incompressible Navier Stokes model for studies of the ocean on parallel computers. *Journal of Geophysical Research* 102: 5753-5766.

Meyers, G., R. J. Bailey, and A. P. Worby. 1995. Geostrophic transport of Indonesian throughflow. *Deep-Sea Research I* 42: 1163-1174.

MIT Climate Modeling Initiative. 2004. *Overview of the Formulation and Numerics of the MIT GCM.* By Adcroft, A., C. Hill, J. Campin and J. Marshall. <http://paoc.mit.edu/cmi/ECMWF2004-Adcroft.pdf>

Papadopoulos, C. 2 August 2005. Estimating the Circulation and Climate of the Ocean (ECCO). <http://www.ecco-group.org/> (1 August 2006).

Stammer, D., C. Wunsch, I. Fukumori, and J. Marshall. 2002a. State Estimation Improves Prospects for Ocean Research. *Eos* 84: 280, 294-295.

Stammer, D., C. Wunsch, R. Giering, C. Eckert, P. Heimbach, J. Marotzke, A. Adcroft, C. N. Hill, and J. Marshall. 2002b. Global ocean circulation during 1992-1997, estimated from ocean observations and a general circulation model. *J. Geophys. Res.* 107: 3118.

Stammer, D., C. Wunsch, R. Giering, C. Eckert, P. Heimbach, J. Marotzke, A. Adcroft, C. N. Hill, and J. Marshall. 2003. Volume, heat, and freshwater transports of the global ocean circulation 1993-2000, estimated from a general circulation model constrained by World Ocean Circulation Experiment (WOCE) data. *J. Geophys. Res.* 108: 3007.

The World Ocean Circulation Experiment (WOCE) 1990-2002. <http://www.soc.soton.ac.uk/OTHERS/woceipo/> (1 August 2006).

Vranes, K., A. L. Gordon, and A. Ffield. 2002. The heat transport of the Indonesian throughflow and implications for the Indian ocean heat budget. *Deep-Sea Research II.* 49: 1391-1410.

Warren, B. A. 1999. Approximating the energy transport across oceanic sections. *J. Geophys. Res.* 104: 7915-1719.

Wunsch, C. 2005. The Total Meridional Heat Flux and Its Oceanic and Atmospheric Partition. *Journal of Climate* 18: 4374-4380.

Wunsch, C., and P. Heimbach. 2006. Estimated Decadal Changes in the North Atlantic Meridional Overturning Circulation and Heat Flux 1993-2004. Manuscript submitted for publication.